

1
2
3
4
5
6
7
8
9
10
11
12
13
14
15
16
17
18
19
20
21
22
23
24
25
26
27

EXPERIMENTAL VERIFICATION OF A BEAM ELEMENT FOR THIN-WALLED BEAMS WITH TORSION, DISTORTION, AND SHEAR LAG

Francisco Cambronero-Barrientos^{a,*}, Ángel Aragón-Torre^b, José-Antonio
Martínez-Martínez^b, Guillermo Aragón-Torre^c

^a*PhD in Civil Engineering,*

C/ Santo Toribio 9, 5-B, 09003 Burgos, Spain

^b*Department of Civil Engineering, University of Burgos,*

C/ Villadiego s/n 09001 Burgos, Spain

^c*Architect, PhD from the University of Burgos, Burgos, Spain*

Abstract

30
31
32
33
34
35
36
37
38
39
40
41
42
43
44
45
46
47
48
49

Beam-type elements based on the theories of Euler-Bernoulli, Timoshenko, and Vlasov are widely used in civil engineering. However, shell and solid finite elements are often used when the effects on normal stresses of either shear deformation or distortion are considered important. Numerically validated in an earlier study with finite element models for shell-type structures, the same *one-dimensional* finite element model is further developed in this study with a low number of *degrees of freedom per node* that includes all the *structural mechanisms* without using 3D finite element models. Laboratory testing of an instrumented steel box girder is conducted, *to improve* validation of the goodness of fit of the finite element model with real structural behavior.

Keywords: Thin-walled beams, warping, Torsion, Distortion, Shear lag, Finite-element method, Box girder, Bridge deck, Experimental verification

*Corresponding author, email: estructuras@vettones.com

Email addresses: estructuras@vettones.com (Francisco Cambronero-Barrientos), aragont@ubu.es (Ángel Aragón-Torre), jmartinez@ubu.es (José-Antonio Martínez-Martínez), garagontorre@gmail.com (Guillermo Aragón-Torre)

1
2
3
4
5
6
7
8
9
10
11
12
13
14
15
16
17
18
19
20
21
22
23
24
25
26
27
28
29
30
31
32
33
34
35
36
37
38
39
40
41
42
43
44
45
46
47
48
49
50
51
52
53
54
55
56
57
58
59
60
61
62
63
64
65

Contents

1 INTRODUCTION	2
2 DESCRIPTION OF THE PROBLEM	4
3 THEORETICAL RESULTS	5
4 DESCRIPTION OF THE TESTS	11
5 TEST RESULTS	15
5.1 Load case 1. Pure flexion	17
5.2 Load case 2. Flexion-torsion	20
6 CONCLUSIONS	23
APPENDIX A. CROSS-SECTIONAL PROPERTIES	33
APPENDIX B. ELEMENT STIFFNESS MATRIX	33
APPENDIX C. NOTATION	33
REFERENCES	35

1. INTRODUCTION

In 2013, a unidimensional element [1] was developed that included all the structural mechanisms of a thin-walled section, which was applicable to any section profile without restrictions, whether open or closed. It was especially developed for the analysis of road-bridge decks, to obtain better results than those obtained with the *classic Euler-Bernoulli beam*, while circumventing the lengthy calculation times of tridimensional shell and solid models.

The element can be used to model the following structural mechanisms: *bending, torsion, distortion, and shear lag*. It was presented in a previous article in 2017 [2], in which the theory was detailed and the results compared with *shell finite element models*.

In this paper, the aim is to resolve an example with the element that has been developed and to verify the results, principally through a comparison with the measurements taken from laboratory tests. The aim is also to give as much detailed information as possible, in relation to the equations used

1
2
3
4
5
6
7
8
9 in the element, so that the reader can easily reproduce the numeric results
10 of the example.

11 The paper reports further development of an element that has previously
12 been presented [2], so it may at times be difficult to understand without a
13 previous reading of the earlier paper, although we have sought to cover the
14 most important points.
15
16

17 As various related articles have been published since the previous paper
18 in 2013, the most relevant will be reviewed, especially those on *shear lag*,
19 which is a recurrent topic in past publications, because it is the most difficult
20 *structural mechanism* to incorporate in a general way for any section profile.
21 The following review of past papers is presented in chronological order.

22 In 2018 and 2019, Lei Zhang *et al.* [17], [16], [18] presented an element
23 with various uncoupled deformation modes, but limited its use to a section
24 with double symmetry, for which reason it is not in general use.
25
26

27 The *shear-lag effect* has been considered in recent studies. Pan Dan-guang
28 *et al.*, in 2018 [10], approached the solution with a semi-analytic method, for
29 a cantilever girder of variable height with a box section. In 2019, Zuolong
30 Luo *et al.* [9] developed a specialized finite element for a box girder. The
31 field of displacement of each section was interpolated with the displacements
32 of various nodes of the upper flange. In 2019, Guo Zengwei *et al.* [3] wrote
33 an article on a theoretical development for the study of the *shear-lag effect*
34 in cantilever box girders of variable depth.
35
36

37 In the interesting work of Minyao Tan and Wenming Cheng [11] in 2019,
38 flexural, torsional and distortional deformation modes were considered. The
39 study was centered on the non-linear behavior of *thin-walled box girders of*
40 *unequal thickness*, although no consideration was given to the *shear-lag effect*,
41 which is one of the important points that is treated in the present study. In
42 their following work [12], the *shear-lag effect* was included, but a parabola
43 was adopted for the warping function, which was only valid for a *single-cell*
44 *box girder*.
45
46

47 Among recent articles closely related with the topic of the present paper
48 is one from 2020 by Ioannis N. Tsiptsis and Olga E. Sapountzaki [13], in
49 continuation of an earlier one of theirs [14]. The deformation modes of the
50 section were obtained with the eigenvalues of a discretization of the cross
51 section through the *Boundary Element Method*, and *isogeometric tools* inte-
52 grated in FEM were used in the longitudinal direction. By doing so, all the
53 deformation modes for an *arbitrary cross section* were included. The defor-
54 mation modes were obtained as eigenvalues, so that they could not be directly
55
56
57
58
59
60
61
62
63
64
65

1
2
3
4
5
6
7
8
9 identified with classic deformation modes: *bending, shear-lag effect, homo-*
10 *geneous and non-homogeneous torsion, homogeneous and non-homogeneous*
11 *distortion*. This objective is one that we are seeking to achieve, because the
12 results, as a composition of all those values, are of immense assistance for un-
13 derstanding the structural behavior of girders and for applying the structural
14 norms that always refer to those modes.

15
16 In 2020, Wen Ying *and* Chen Ze-lin [15] defined a *one-dimensional finite*
17 *element* for the *analysis of warping torsion*, but without including either the
18 *shear-lag effect or distortion*.

19
20 In 2020 [7], Xiayuan Li *et al.* developed a *formulation for a finite beam*
21 *element* for *torsional analysis in thin-walled single or multi-cell box girders*
22 and, in 2021 [8], they developed another for *considering shear-lag, and shear-*
23 *deformation effects*. In both papers, one of the examples was taken from
24 [2]. However, the distortion resulting from only loading one of webs, taken
25 from the original example of a *bridge deck with a three-cell section*, was not
26 included in their study, so the authors were unable to reproduce the geometric
27 and load distribution plans of that example.

31 32 33 34 35 36 37 38 39 40 41 42 43 44 45 46 47 48 49 50 51 52 53 54 55 56 57 58 59 60 61 62 63 64 65

As indicated in the introduction, the aim was to conduct laboratory tests on a girder under two different loading states and to compare the measured values with those obtained using the unidimensional finite element model reported in this paper. The geometry of the chosen section shown in Figure (1) consisted of a box section with a total width of $b = 1.0(m)$, two flanges of $b/4 = 0.25(m)$ in length, with a distance of $b/4 = 0.25(m)$ between the midpoints of the *top and the bottom flanges*, built of *S275JR* steel plating with a thickness of $t = 8(mm)$. The girder with this section was placed between the supporting points, $L = 4.0(m)$. Steel diaphragms of the same thickness were inserted to avoid distortion of the section due to supports, and no diaphragm at intermediary points, so that the influence of any distortion was as high as possible, and so that its effect could be measured in the tests.

The first load distribution, shown in Figure (2), was formed of 4 forces with the following values, $F_y = 20.0(kN)$, situated transversely across the webs, to avoid transverse flexion of the section and longitudinally, $L_c = 0.30(m)$, in two pairs, so that there was no loading of the instrumentation for the tests within the central section of the girder. With these loads, the aim was to confirm a state in which there will be flexion without either torsion

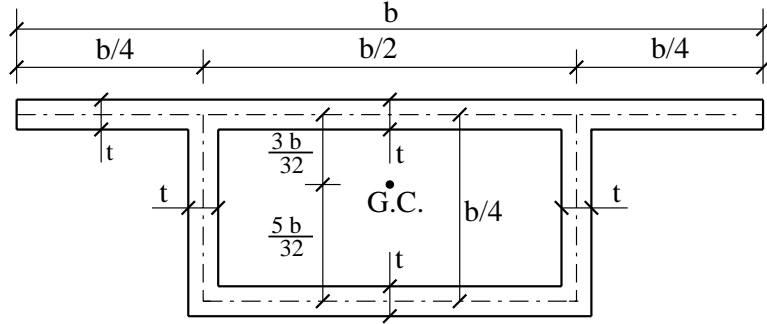


Figure 1: Geometry of box-shaped cross-section and Gravity center (G.C.) $b = 1000$ (mm), $t = 8$ (mm).

or distortion, in which the distribution of stress at the girder center will be greatly influenced by the shear-lag effect.

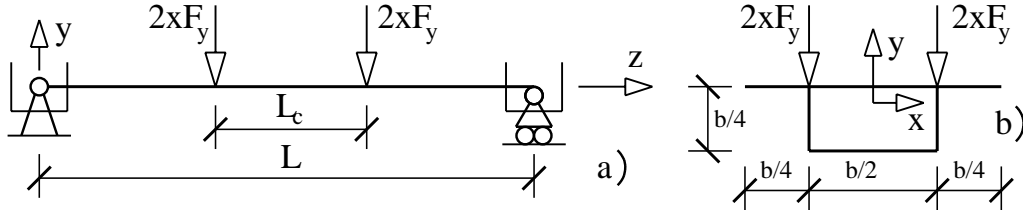


Figure 2: Bending: single-cell simple-span. $L = 4.0$ (m) , $L_c = 0.30$ (m) , $F_y = 20.0$ (kN) , $b = 1.0$ (m).

With the second load distribution depicted in Figure (3), the aim was to confirm a loading state with torsion and distortion, which may appear in combination with some measure of flexion. It is the same as the preceding case, except that the loading on one of the webs reduced its value to $1/4$ of the other loading state. A loading pattern without any flexion was discounted, as in reality it could hardly occur in a road bridge and because the performance of the test was more difficult as it was statically more unstable, without having to prevent the displacement of a support.

3. THEORETICAL RESULTS

The first step to complete the theoretical calculation was to define the deformation modes that were subsequently combined to form the displacement fields. The methodology developed by Jeppe Jönsson [4] was followed

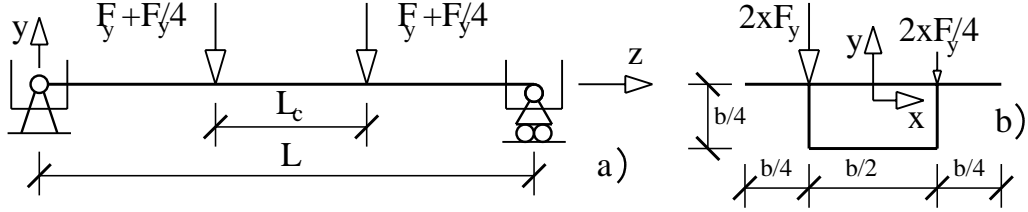


Figure 3: Torsion-distortion: Simple supported girder. $L = 4.0$ (m) , $L_c = 0.30$ (m) , $F_y = 20.0$ (kN) , $b = 1.0$ (m).

to define the displacement fields, through a *finite element with two nodes*, each with a degree of freedom that represented the warp of the node, using linear functions to interpolate within the finite element. It is a very simple methodology to apply and is valid for any form of thin-walled section, whether open or closed. The exact solution can be obtained through the appropriate choice of form functions, as shown in [1]. The deformation modes that were obtained for the test section of the girder are shown in Appendix A.

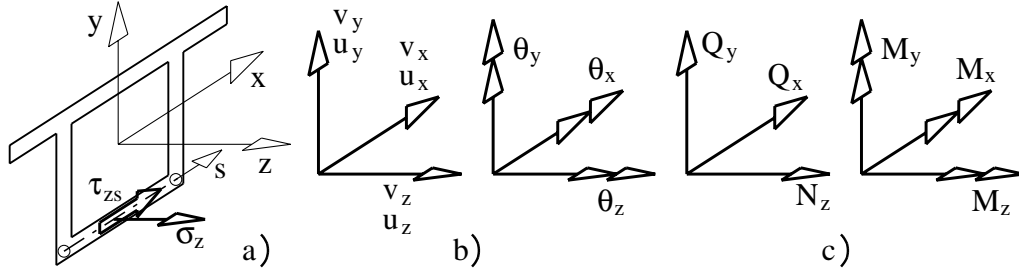


Figure 4: Notations: a) for stresses; b) for displacements and rotations; c) for internal forces.

In Figure (4), the notation and the conventional signs used to denote displacements, rotations, and forces are depicted. On these axes, the displacement field is the sum of the fields corresponding to all of the resistance modes under consideration and is given by Equation (1). The description of each summand is the following:

- (u_x, u_y, u_z) are the displacements of the girder axis, due to *bending* and *axial force*.
- $(-(y - y_a) \cdot \theta_z, +(x - x_a) \cdot \theta_z)$ displacements of a point (x, y) , due to the rotation, θ_z , of a rigid solid around the *shear center*, (x_a, y_a) .

- $(u_{dx} \cdot \psi_d, u_{dy} \cdot \psi_d)$ displacements on the plane of the section, due to distortion where ψ_d is the intensity of the distortion.
- $(-y \cdot \frac{du_y}{dz} - x \cdot \frac{du_x}{dz})$ is the longitudinal displacement due to flexural rotation.
- $(w_y \cdot \frac{Q_y}{G_o} + w_x \cdot \frac{Q_x}{G_o})$ is *warping*, due to the *shear-lag effect* as a result of *shear forces*.
- $(+w_a \cdot \frac{d\theta_z}{dz} + w_{at} \cdot \frac{d^3\theta_z}{dz^3})$ is the *warping*, due to homogeneous and non-homogeneous torsion.
- $(-w_d \cdot \frac{d\psi_d}{dz} + w_{dt} \cdot \frac{d^3\psi_d}{dz^3})$ is *warping*, due to homogeneous and non-homogeneous distortion.

$$\left. \begin{aligned} v_x(x, y, z) &= u_x - (y - y_a) \cdot \theta_z + u_{dx} \cdot \psi_d \\ v_y(x, y, z) &= u_y + (x - x_a) \cdot \theta_z + u_{dy} \cdot \psi_d \\ v_z(x, y, z) &= u_z - y \cdot \frac{du_y}{dz} + w_y \cdot \frac{Q_y}{G_o} - x \cdot \frac{du_x}{dz} + w_x \cdot \frac{Q_x}{G_o} \\ &\quad + w_a \cdot \frac{d\theta_z}{dz} + w_{at} \cdot \frac{d^3\theta_z}{dz^3} - w_d \cdot \frac{d\psi_d}{dz} + w_{dt} \cdot \frac{d^3\psi_d}{dz^3} \end{aligned} \right\} \quad (1)$$

This displacement field presents the problem that the forces, Q_x and Q_y , which are in principle unknown until the results are obtained, multiply the *warping due to shear forces*. The most novel aspect of the unidimensional finite element that has been developed is its capability to eliminate these forces from the displacement field. It is done by defining new warping functions that are orthogonal to the flexural rotations of the section. For example, in the case of shear stress, Q_y , the new warping function, $w_y = C_{y_o} \cdot y + w_{y_o}$, was defined and the constant, C_{y_o} , of the orthogonality condition, $\int_A w_{y_o} y dA = 0$, was obtained. This breakdown is represented in Figure (5), in which the original warping function is broken down into a rotation of the whole section in which it remains flat and then actual warping in the strict sense of the term, meaning that the section is no longer flat. The method of performing this

1
2
3
4
5
6
7
8
9
10
11
12
13
14
15
16
17
18
19
20
21
22
23
24
25
26
27
28
29
30
31
32
33
34
35
36
37
38
39
40
41
42
43
44
45
46
47
48
49
50
51
52
53
54
55
56
57
58
59
60
61
62
63
64
65

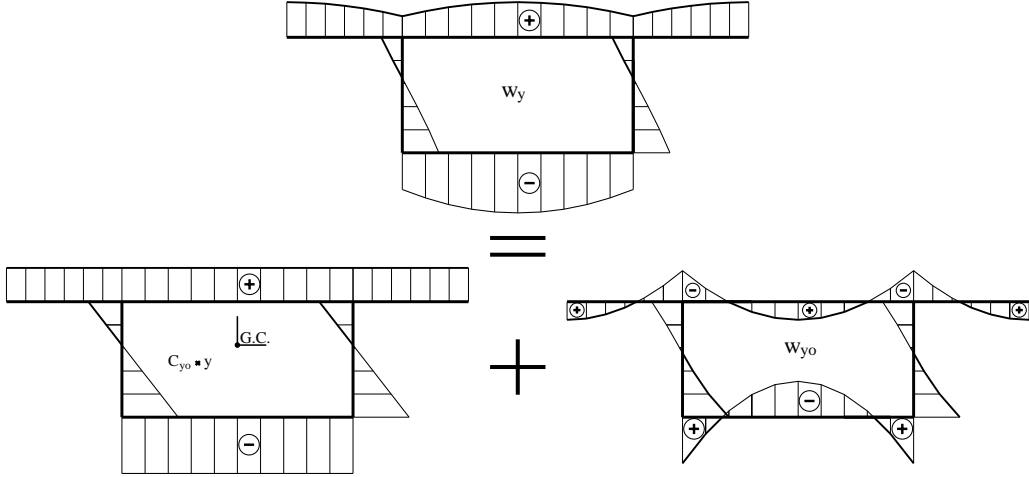


Figure 5: Breakdown of shear-related warping, w_y

breakdown is valid for any sectional form, unlike many other authors whose use of predefined functions are only valid for specific sectional forms.

The displacement field is rewritten with warping functions according to the equation (2). The shear forces, Q_x and Q_y , disappear and are substituted by two intensities of shear-related warping, χ_x and χ_y , and two constants are introduced, A_x and A_y , which although not strictly necessary represent the areas of shearing, so that the intensities of shear-related warping have no units. In Figure (6), the displacement field is shown on the plane that contains the section and the displacement outside the plane of the section is represented in Figure (7).

$$\left. \begin{aligned}
 v_x(x, y, z) &= u_x - (y - y_a) \cdot \theta_z + u_{dx} \cdot \psi_d \\
 v_y(x, y, z) &= u_y + (x - x_a) \cdot \theta_z + u_{dy} \cdot \psi_d \\
 v_z(x, y, z) &= u_z + y \cdot \theta_x + w_{y_0} \cdot A_y \cdot \chi_y - x \cdot \theta_y + w_{x_0} \cdot A_x \cdot \chi_x \\
 &\quad + w_a \cdot \frac{d\theta_z}{dz} + w_{at} \cdot \frac{d^3\theta_z}{dz^3} - w_d \cdot \frac{d\psi_d}{dz} + w_{dt} \cdot \frac{d^3\psi_d}{dz^3}
 \end{aligned} \right\} \quad (2)$$

The rigidity matrix of a finite element can be obtained from this displacement field with the standard methodology. Full details may be found in [2], while only a brief summary is given in the present article.

Longitudinal strain, ϵ_z , is found with Equation (3), and multiplying by the *Young's modulus* yields the longitudinal stress, $\sigma_z = E \cdot \epsilon_z$. *The transverse*

1
2
3
4
5
6
7
8
9
10
11
12
13
14
15
16
17
18
19
20
21
22
23
24
25
26
27
28
29
30
31
32
33
34
35
36
37
38
39
40
41
42
43
44
45
46
47
48
49
50
51
52
53
54
55
56
57
58
59
60
61
62
63
64
65

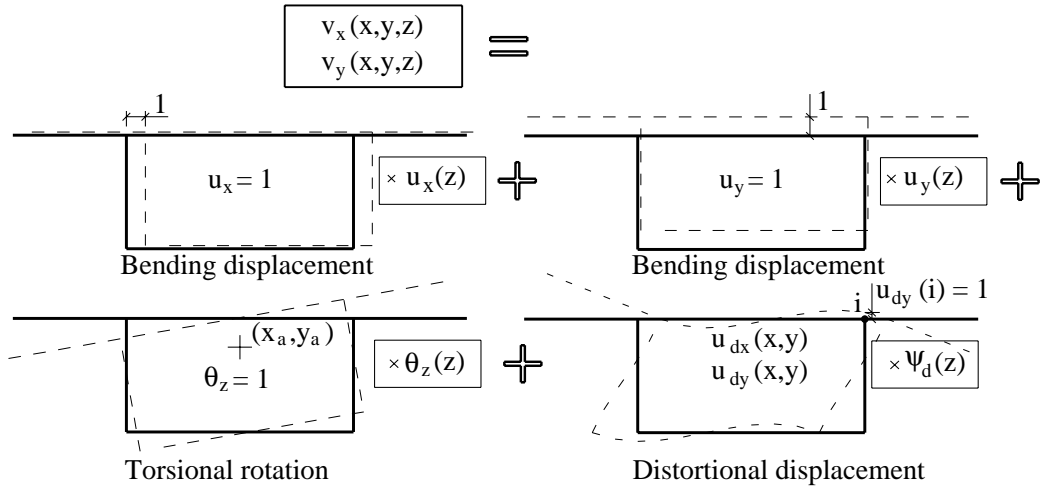


Figure 6: Displacement field: $v_x(x, y, z)$, $v_y(x, y, z)$.

strain, γ_{zs} , given by equation (4) is multiplied by the elastic shear modulus to obtain the shear stress, $\tau_{zs} = G \cdot \gamma_{zs}$. The terms that appear with a high order of derivation are neglected.

$$\begin{aligned}
 \epsilon_z = \frac{\partial v_z}{\partial z} = & \frac{du_z}{dz} + && \text{Axial } N_z \\
 & + \left(+y \cdot \frac{d\theta_x}{dz} + w_{yo} \cdot A_y \cdot \frac{d\chi_y}{dz} \right) && \text{Moment } M_x \\
 & + \left(-x \cdot \frac{d\theta_y}{dz} + w_{xo} \cdot A_x \cdot \frac{d\chi_x}{dz} \right) && \text{Moment } M_y \\
 & + \left(+w_a \cdot \frac{d^2\theta_z}{dz^2} + \cancel{w_{at} \cdot \frac{d^4\theta_z}{dz^4}} \right) && \text{Torsion} \\
 & + \left(-w_d \cdot \frac{d^2\psi_d}{dz^2} + \cancel{w_{dt} \cdot \frac{d^4\psi_d}{dz^4}} \right) && \text{Distortion}
 \end{aligned} \tag{3}$$

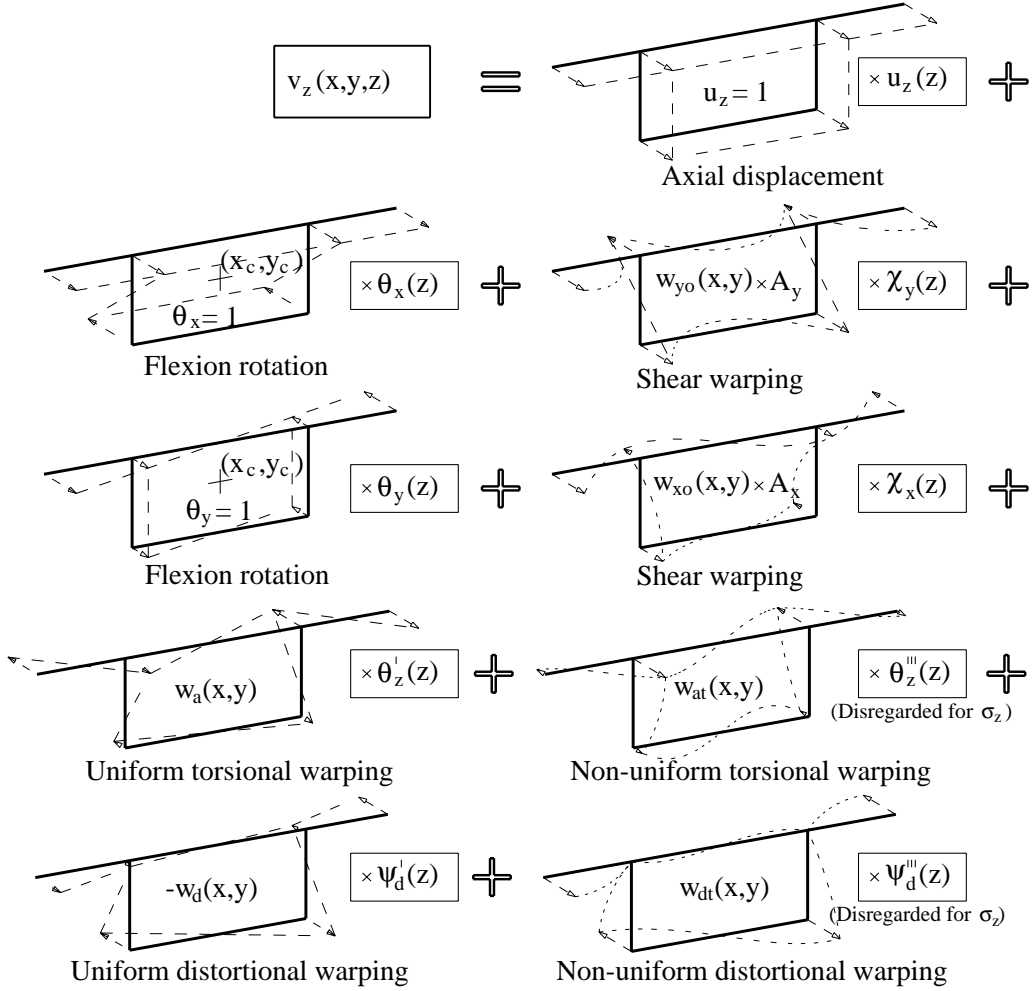


Figure 7: Displacement field: $v_z(x, y, z)$.

43
44
45
46
47
48
49
50
51
52
53
54
55
56
57
58
59
60
61
62
63
64
65

$$\begin{aligned}
 \gamma_{zs} &= \frac{\partial v_s}{\partial z} + \frac{\partial v_z}{\partial s} = t_x \frac{\partial v_x}{\partial z} + t_y \frac{\partial v_y}{\partial z} + \frac{\partial v_z}{\partial s} \\
 &= \left(t_x \left(\frac{du_x}{dz} - \theta_y \right) + \frac{\partial w_{xo}}{\partial s} A_x \chi_x \right) \text{ Shear } Q_x \\
 &+ \left(t_y \left(\frac{du_y}{dz} + \theta_x \right) + \frac{\partial w_{yo}}{\partial s} A_y \chi_y \right) \text{ Shear } Q_y \\
 &+ \left(\frac{\partial w_a}{\partial s} - h_a \right) \frac{d\theta_z}{dz} + \frac{\partial w_{at}}{\partial s} \frac{d^3\theta_z}{dz^3} \text{ Torsion} \\
 &+ \left(u_{ds} - \frac{\partial w_d}{\partial s} \right) \frac{d\psi_d}{dz} + \frac{\partial w_{dt}}{\partial s} \frac{d^3\psi_d}{dz^3} \text{ Distortion}
 \end{aligned}$$

10

(4)

1
2
3
4
5
6
7
8
9
10
11
12
13
14
15
16
17
18
19
20
21
22
23
24
25
26
27
28
29
30
31
32
33
34
35
36
37
38
39
40
41
42
43
44
45
46
47
48
49
50
51
52
53
54
55
56
57
58
59
60
61
62
63
64
65

The strain energy was obtained through the sum of the following three terms: strain energy density from longitudinal stress, $dU_\epsilon/dz = 1/2 \int_A E \epsilon_z^2 dA$; strain energy density from shear stress, $dU_\gamma/dz = 1/2 \int_A G \gamma_{zs}^2 dA$; and strain energy density in terms of distortion displacement mode on the cross sectional plane, $dU_{K_d}/dz = 1/2 E_o K_d \psi_d^2$.

Displacement and its first derivative have their degrees of freedom in relation to torsional rotations and distortional displacement. Only the value of the displacement is necessary for the other unknown functions, so a total of eleven degrees of freedom are needed for each node.

- Displacements: $\mathbf{u}_{xi}, \mathbf{u}_{yi}, \mathbf{u}_{zi}$
- Rotations: $\theta_{xi}, \theta_{yi}, \theta_{zi}$
- Derivative of torsional rotation: θ'_{zi}
- Warp intensities: χ_{xi}, χ_{yi}
- Distortional displacement: ψ_d
- Derivative of distortional displacement: ψ'_d

Having selected a three-node element, two at each end and one in the center, the *shape functions* are all second-degree polynomials, except for the degrees of freedom in which their derivatives as such also appear where third-degree polynomials are employed. *Minimizing the total potential energy* yielded the *stiffness matrix*, whose equation may be found in Appendix B. In the rigidity matrix, the terms that link bending with torsion and distortion, and the terms that link bending on the z-x plane with bending on the z-y plane were discarded.

Having set out the finite element problem in this way, the 4-meter long girder was divided into 80 *one-dimensional finite elements*, which were numerically resolved for the two proposed loading states. The results for stresses are included in the tables in which they are compared with values measured in the tests.

4. DESCRIPTION OF THE TESTS

Tests were performed on a box girder supported at both ends, by applying four separate loads within the central zone of the girder, in order to contrast the experimental with the theoretical results. The first test was completed

1
2
3
4
5
6
7
8
9 with the application of four separate loads (Figure 2), up to a maximum
10 value of 20 kN. In the second test, four separate loads were also applied,
11 but of different values, two by two (Figure 3), on one side, two loads up to the
12 same maximum value of 20 kN, and, on the other, two loads to a value of
13 5 kN.
14

15 We will describe the test processes themselves. In the first place, the
16 box girder was placed upon two *trestles* at a distance of 4 meters from each
17 other, ensuring that the center of the girder coincided with the position of
18 the actuator, as shown in Figure 8.
19
20



48
49
50
51
52
53
54
55
56
57
58
59
60
61
62
63
64
65

Figure 8: General overview of test.

An *MTS* 244.41 dynamic actuator was used, with a capacity of 500 kN; a piston depth of 150 mm; two servovalves, each of 56 liters/min; a double-effect actuator (Traction/Compression); and options for load control (*MTS* 6661.25 F.01 500 kN capacity cell and a non-linearity of 0.15%) and displacement. The actuator was connected to a central hydraulic system (*MTS*) with a

1
2
3
4
5
6
7
8
9 hydraulic fluid impulsion capacity of 200 liters per minute at a pressure of
10 20 MPa, and an integrated cooling system. FlextestGT actuator control
11 software (MTS brand) was used.
12

13 The next step was to position the four load cells, separated at intervals of
14 30 cm along the length of the girder, at intervals of 50 cm in the transverse
15 direction, so that they coincided with the webs of the box girder. To do so,
16 the load cells were bolted two by two to a profile, maintaining the distance
17 between them at 30 cm, and both profiles each with two load cells were subse-
18 quently positioned lengthwise on the box girder. Finally, another profile was
19 placed in a transverse direction to the direction of the actuator load (Figure
20 9). The four load cells were Sensocar brand-type CR – 1 de 5000 kg (50 kN),
21 with a sensitivity of $2 \pm 0.1\%$ mv/V.
22
23
24



52 Figure 9: Detail of load cells.
53

54 The HBM brand Linear Variable Differential Transformers (LVDTs) with
55 a range of 50 mm and with a linear error of 0.1% at the bottom of the scale)
56
57
58
59
60
61
62
63
64
65

1
2
3
4
5
6
7
8
9
10
11
12
13
14
15
16
17
18
19
20
21
22
23
24
25
26
27
28
29
30
31
32
33
34
35
36
37
38
39
40
41
42
43
44
45
46
47
48
49
50
51
52
53
54
55
56
57
58
59
60
61
62
63
64
65

were positioned midspan, at one third and at one quarter of the span, and on the supports (Figure 10).

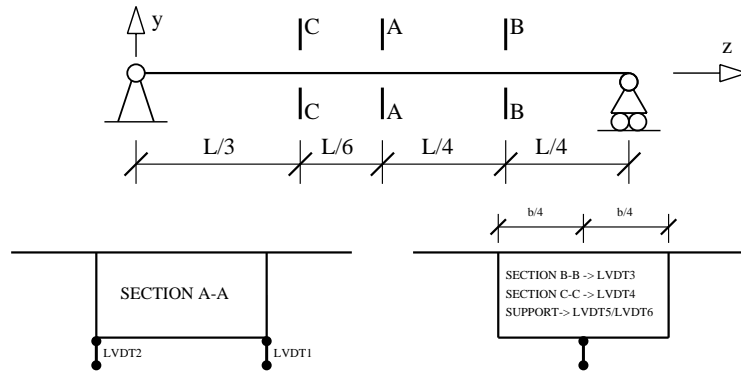


Figure 10: Instrumentation for measurement of displacements.

Prior to the whole process of preparing the test, the extensometric bands had been adhered to the girder ($FLA-6-11-1L$, 120Ω , and 6 mm in length; from Figure 11). All that remained to do was to connect the data-acquisition module, an HBM brand *QuantumX MX1615B*, in other words the load cells, LVDTs, extensometric bands and actuator. HBM brand Catman data-acquisition software was used, with which we recorded the signals of all the elements that were connected (using a recording frequency of 5 Hz , in other words, 5 datums per second).

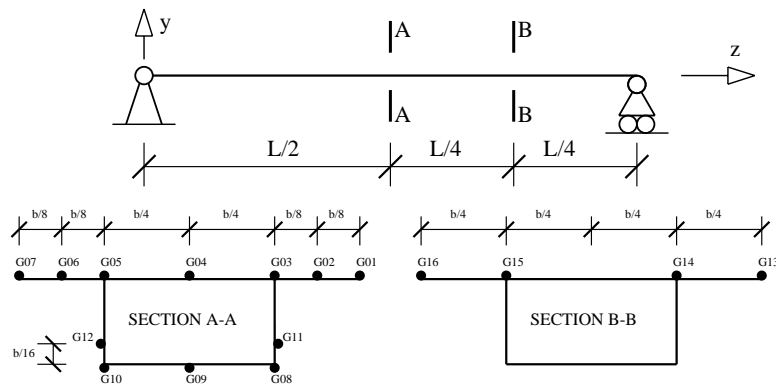


Figure 11: Instrumentation for measurement of deformations.

The process of carrying out the test relied on the load actuator control,

1
2
3
4
5
6
7
8
9 with stepped increases, to verify the correct application of the four separate
10 loads according to the type of test. At all times, the data that the load cells,
11 LVDTs, extensometric bands and actuator were recording were displayed on
12 a screen. The load application graphs of each cell with which the exact
13 application of load was controlled are shown in Figures 12 and 13.
14

15 Whereas the girder geometry, the positions of the loads, and their values
16 were perfect in the numeric models, the reality was very different. The girder
17 geometry was not perfect and when supported on four points with loading
18 applied at another four, it is very difficult to situate the four points on the
19 same plane, for which reason it is impossible to achieve test loads that are
20 exactly as desired. However, as may be seen in the aforementioned graphs,
21 the loads were very close to the desired amounts.
22

23 Before starting to apply the load, all the instrumentation was initialized
24 with zero values, for which reason the own weight of the girder and the other
25 test accessories had no effect on the measured results, as they had previously
26 been applied. As the tensile tests were in an elastic regime, the average
27 deformations were converted into stress, multiplying them by the modulus of
28 elasticity of steel, for which a value of $E = 210000 (N/mm^2)$ was adopted.
29 As the measurement precision was $1 \mu m/m$, the error in the measurement of
30 tensile stress was $1e^{-6} * 210000 = 0.21(N/mm^2)$
31

32 The test was repeated on various occasions with no significative differ-
33 ences between the values that were obtained.
34
35
36

37 38 39 **5. TEST RESULTS** 40 41 42 43 44 45 46 47 48 49 50 51 52 53 54 55 56 57 58 59 60 61 62 63 64 65

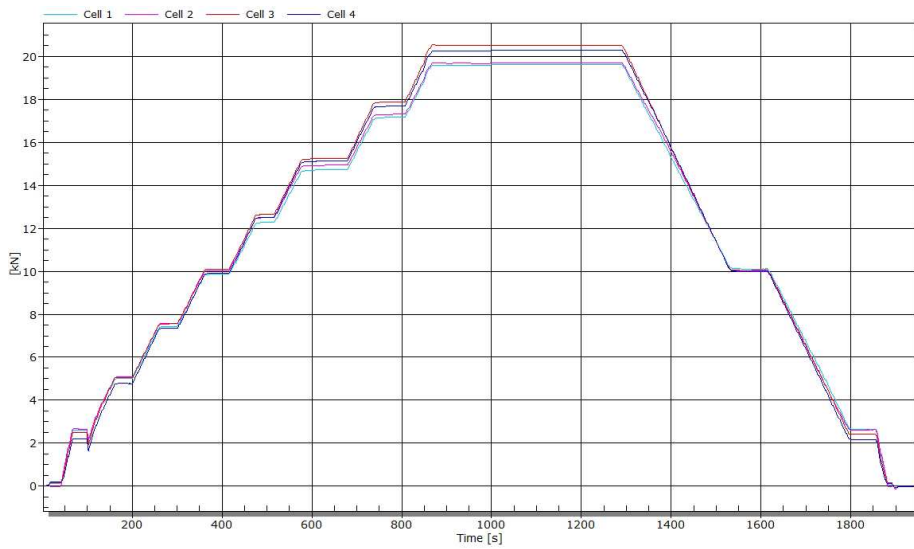


Figure 12: Case 1 Pure Flexion. Load on each cell as a function of time.

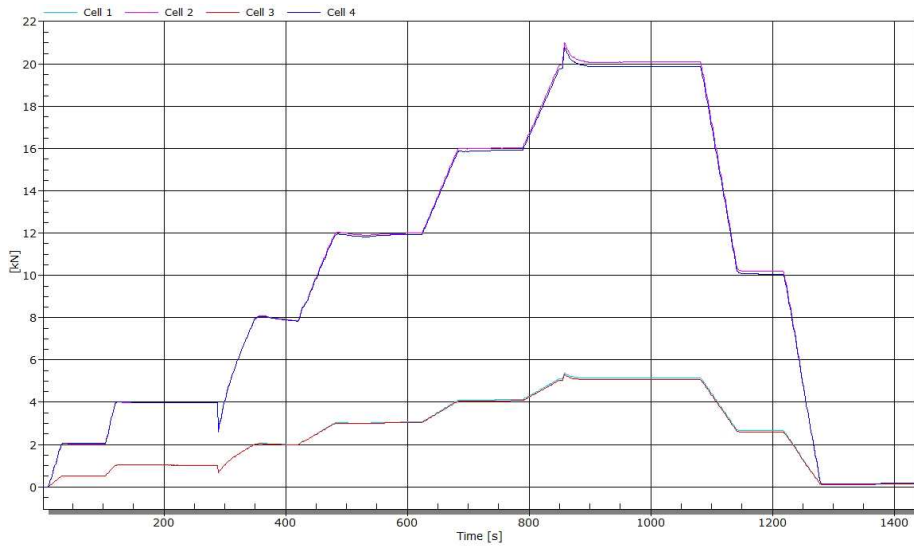


Figure 13: Case 2 Flexion-torsion. Load on each cell as a function of time

1
2
3
4
5
6
7
8
9
10
11
12
13
14
15
16
17
18
19
20
21
22
23
24
25
26
27
28
29
30
31
32
33
34
35
36
37
38
39
40
41
42
43
44
45
46
47
48
49
50
51
52
53
54
55
56
57
58
59
60
61
62
63
64
65

5.1. Load case 1. Pure flexion

As indicated, the load was arranged in the first test, so that no torsion and only flexural stress was produced. In the following table, the stresses in the midspan section in the tests are compared with those of the numerical calculations, both at N/mm^2 . The rows of Table A correspond to the following values obtained with: the unidimensional finite element proposed by the authors (B3N); a layer-type Finite Element (FEM) Model; the (classic) Euler-Bernoulli theory for reference purposes, in order to note the variation in values, due to the *shear-lag effect*; and the average test values.

$z = L/2$	Method	$-b/2$	$-b \cdot 3/8$	$-b/4$	0	$+b/4$	$+b \cdot 3/8$	$+b/2$
<i>Top flange</i>	B3N	-34.6	-35.5	-38.4	-34.6	-38.4	-35.5	-34.6
	<i>FEM</i>	-32.9	-34.9	-36.8	-34.8	-36.8	-34.9	-32.9
	<i>Classic</i>	-37.2	-37.2	-37.2	-37.2	-37.2	-37.2	-37.2
	<i>Test</i>	-36.2	-37.4	-38.1	-35.8	-37.9	-36.4	-37.3
<i>Bottom flange</i>	B3N			63.6	57.2	63.6		
	<i>FEM</i>			64.1	57.6	64.1		
	<i>Classic</i>			62.3	62.3	62.3		
	<i>Test</i>			65.9	54.6	67.4		

The values of the table are drawn in Figure 14. There was a slight anomaly in the *top flange* during the test, in which the value measured at one end ($37.3 N/mm^2$) was slightly higher than at the center of the flange ($36.4 N/mm^2$). This anomaly reoccurred in all repetitions of the test, possibly due to the fact that the tests on the geometry of the girder and the loads were never quite perfect. The average measured value in $\pm b/4$ of $-38.1 N/mm^2$ coincided very closely with the one obtained with the unidimensional finite element, $-38.4 N/mm^2$, showing a difference of only 1.0%.

The value measured at the center of the *bottom flange* was lower than all those obtained with numerical calculations, and in compensation the maximum measured value was greater than the other values. The average measured value, $+66.7 N/mm^2$ at each end, was 4.8% higher than the value obtained with the finite element, $+63.6 N/mm^2$ (B3N), for which reason the coincidence was very good for the maximum stress level in this loading state.

The following table lists the stress values at (N/mm^2) for the section within the first quarter of the *span*. As it is a section at some distance from the load application point, the stress variations in the width of the section, due to the *shear-lag effect* was small. It never happened in this section,

1
2
3
4
5
6
7
8
9
10
11
12
13
14
15
16
17
18
19
20
21
22
23
24
25
26
27
28
29
30
31
32
33
34
35
36
37
38
39
40
41
42
43
44
45
46
47
48
49
50
51
52
53
54
55
56
57
58
59
60
61
62
63
64
65

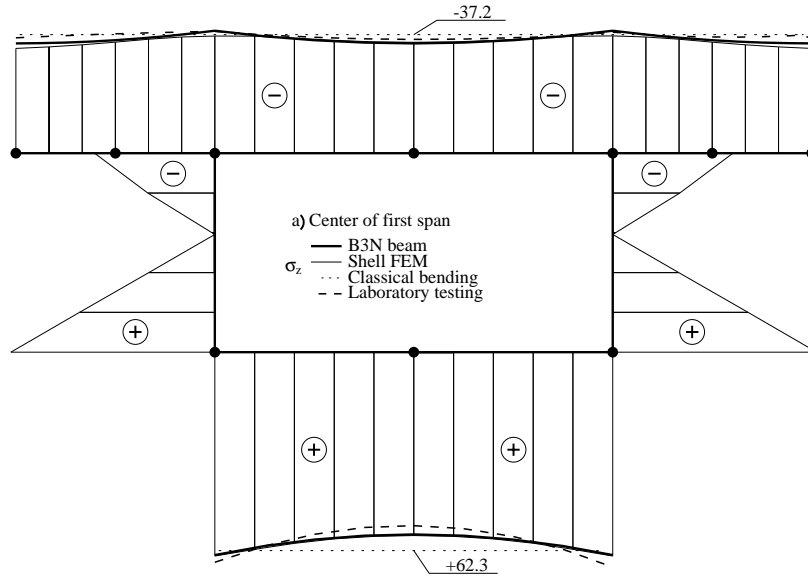


Figure 14: Case 1 Pure flexion. Stresses at midspan in (N/mm^2)

because the maximum measured value was at one end of the *top flange*, although it could be seen that the 2 values on one side were slightly higher than the 2 values on the other side. In $\pm b/4$, the average value of the measurements, $-20.8N/mm^2$, was 6.7% higher than the value obtained with the unidimensional element, *B3N*.

$z = L/4$	Method	$-b/2$	$-b \cdot 3/8$	$-b/4$	0	$+b/4$	$+b \cdot 3/8$	$+b/2$
<i>Top flange</i>	B3N	-19.5	-19.5	-19.5	-19.5	-19.5	-19.5	-19.5
	<i>FEM</i>	-19.5	-19.4	-19.5	-19.4	-19.5	-19.4	-19.5
	<i>Classic</i>	-20.1	-20.1	-20.1	-20.1	-20.1	-20.1	-20.1
	<i>Test</i>	-19.7	--	-21.2	--	-20.4	--	-18.0
<i>Bottom flange</i>	B3N			32.4	32.4	32.4		
	<i>FEM</i>			32.4	32.4	32.4		
	<i>Classic</i>			33.7	33.7	33.7		
	<i>Test</i>			--	--	--		

It may be seen from the values shown in figure 15 that in practice all the values were superimposed on a constant distribution across the width of the section.

A comparison of the average displacements at three points on the girder

1
2
3
4
5
6
7
8
9
10
11
12
13
14
15
16
17
18
19
20
21
22
23
24
25
26
27
28
29
30
31
32
33
34
35
36
37
38
39
40
41
42
43
44
45
46
47
48
49
50
51
52
53
54
55
56
57
58
59
60
61
62
63
64
65

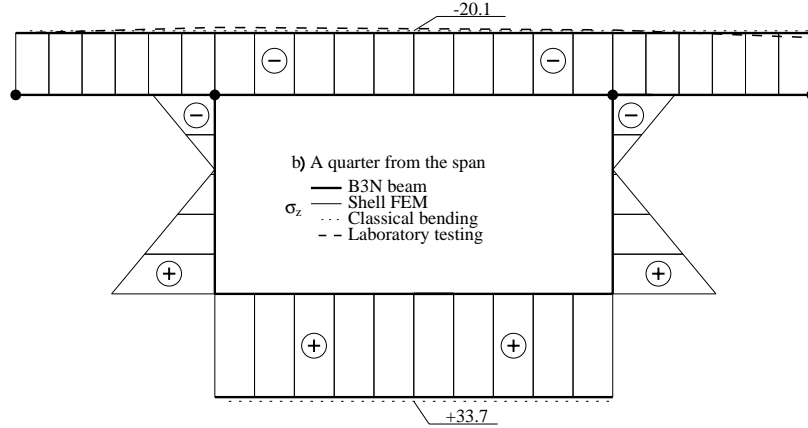


Figure 15: Case 1 Pure flexion. Stresses at quarter span in (N/mm^2).

is presented in the following table, in order to complete the analysis of measurements resulting from this loading state.

The average center-span values, $\pm 3.4\%$, coincided with the average measurements. The measured displacement was somewhat higher than at other points, but the difference was not sufficiently significant for the presence of torsion generated by the applied loads to be noted. In the section within the first quarter of the *span*, the average value was 5% higher than calculated. The Bernoulli (Classic) theory yielded lower values, as shear deformation was not considered.

$z =$	$L/2$	$L/2$	$L/4$
$x =$	$-b/4$	$+b/4$	0
B3N	-2.9	-2.9	-2.0
<i>FEM</i>	-2.9	-2.9	-2.0
<i>Classic</i>	-2.4	-2.4	-1.7
<i>Test</i>	-3.0	-2.8	-2.1

Displacement on the girder supports was also measured during the test. The measured values shown in the above table were corrected, so that they reflected the displacement from the line that joins the supporting points.

1
2
3
4
5
6
7
8
9
10
11
12
13
14
15
16
17
18
19
20
21
22
23
24
25
26
27
28
29
30
31
32
33
34
35
36
37
38
39
40
41
42
43
44
45
46
47
48
49
50
51
52
53
54
55
56
57
58
59
60
61
62
63
64
65

5.2. Load case 2. Flexion-torsion

The second combination of loads used to test the girder generated both flexion and torsion in equal quantities. A laboratory controlled application of a state in which there is only torsion is difficult without a special custom-built tool with which to apply the load and to adjust the supports. To do so, some loads were applied to produce torsion, but that maintained all the supporting points under compression.

The following table shows a comparison between the average values, both measured and calculated, that are shown in Figure 16. The values with the classic theory of beams include no *warping torsion*, nor *shear-lag effect*, for which reason the stresses are considered constant throughout the width and are included only as a reference. In the *top flange*, the maximum measured stress, $-31.1 N/mm^2$, was 1.0% higher than the value, $-30.8 N/mm^2$, obtained with the unidimensional element, *B3N*. The minimum calculated value at the other end of the *top flange* was 12.9% lower than the average value.

At the *bottom flange*, as in the case of the above load, the value measured at the center of the girder was somewhat lower than the calculated values. The maximum calculated value of $+59.3 N/mm^2$ was 0.5% lower than the average value of $+59.6 N/mm^2$.

$z = L/2$	Method	$-b/2$	$-b \cdot 3/8$	$-b/4$	0	$+b/4$	$+b \cdot 3/8$	$+b/2$
<i>Top flange</i>	B3N	-30.8	-29.7	-29.7	-21.6	-18.3	-14.7	-12.4
	<i>FEM</i>	-28.4	-28.4	-28.3	-21.8	-17.7	-15.2	-12.8
	<i>Classic</i>	-23.3	-23.3	-23.3	-23.3	-23.3	-23.3	-23.3
	<i>Test</i>	-31.1	-30.6	-29.4	-22.6	-18.5	-15.8	-14.0
<i>Bottom flange</i>	B3N			59.3	35.7	20.3		
	<i>FEM</i>			59.0	36.0	21.0		
	<i>Classic</i>			39.0	39.0	39.0		
	<i>Test</i>			59.6	33.2	21.1		

The stresses within the first quarter of the *span* followed a linear distribution, as may be seen below in Figure 17. In the *top flange*, the maximum average stress, $-16.4 N/mm^2$, was not towards the end, which was 4.3% higher than the calculated value of $-15.5 N/mm^2$.

1
2
3
4
5
6
7
8
9
10
11
12
13
14
15
16
17
18
19
20
21
22
23
24
25
26
27
28
29
30
31
32
33
34
35
36
37
38
39
40
41
42
43
44
45
46
47
48
49
50
51
52
53
54
55
56
57
58
59
60
61
62
63
64
65

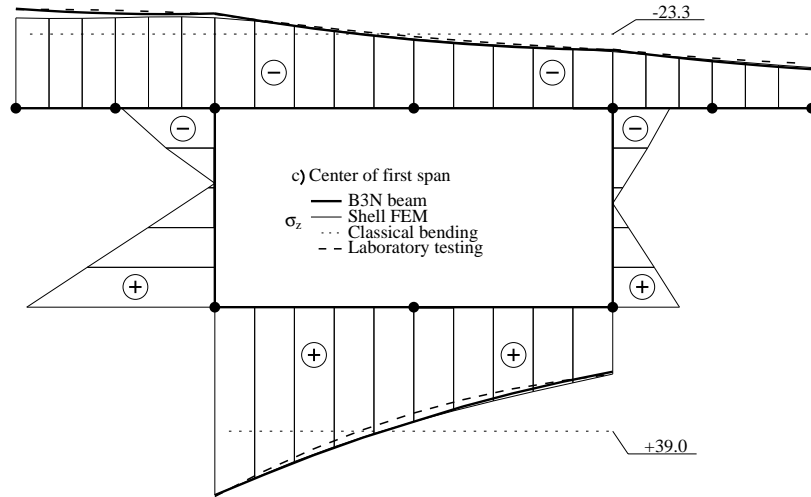


Figure 16: Case 2 Flexion - torsion. Stresses at midspan in (N/mm^2).

$z = L/4$	Method	$-b/2$	$-b \cdot 3/8$	$-b/4$	0	$+b/4$	$+b \cdot 3/8$	$+b/2$
Top flange	B3N	-15.5	-14.7	-13.9	-12.2	-10.5	-9.6	-8.8
	FEM	-15.1	-14.4	-13.5	-12.2	-10.8	-9.9	-9.2
	Classic	-12.6	-12.6	-12.6	-12.6	-12.6	-12.6	-12.6
	Test	-16.2	--	-16.4	--	-12.5	--	-10.8
Bottom flange	B3N			26.7	20.3	13.9		
	FEM			25.7	20.3	14.9		
	Classic			21.1	21.1	21.1		
	Test			--	--	--		

In this combination of loads with torsion, the maximum deflection measured in millimetres was 7% higher than the calculated amount. A similar percentage to the result for the other combination of loads.

1
2
3
4
5
6
7
8
9
10
11
12
13
14
15
16
17
18
19
20
21
22
23
24
25
26
27
28
29
30
31
32
33
34
35
36
37
38
39
40
41
42
43
44
45
46
47
48
49
50
51
52
53
54
55
56
57
58
59
60
61
62
63
64
65

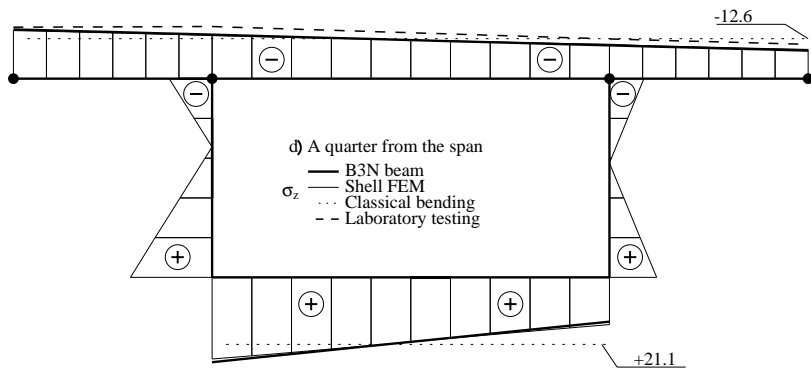


Figure 17: Case 2 Flexion - torsion. Stresses at a quarter span in (N/mm^2) .

$z =$	$L/2$	$L/2$	$L/4$
$x =$	$-b/4$	$+b/4$	0
B3N	-2.40	-1.20	-1.20
<i>FEM</i>	-2.40	-1.20	-1.20
<i>Classic</i>	-1.60	-1.50	-1.00
<i>Test</i>	-2.57	-1.06	-1.20

In addition to yielding total stress, the unidimensional element that was proposed yielded a breakdown by modes that is shown in Figure 18. The flexural mode contributed most to the maximum stress, followed by the distortion mode. Torsion was the mode that contributed least to the total.

Lower error values than the values obtained with the proposed element may be obtained with the calculation models of other authors, for example [8], for particular combinations of loads and section profiles, although those calculation models cannot be used in a general way for any structure and for any combination of loads. The main advantage of the unidimensional element described in this paper is its validity for any section profile and for any loading state, such that it can be used in a general way for design in civil engineering.

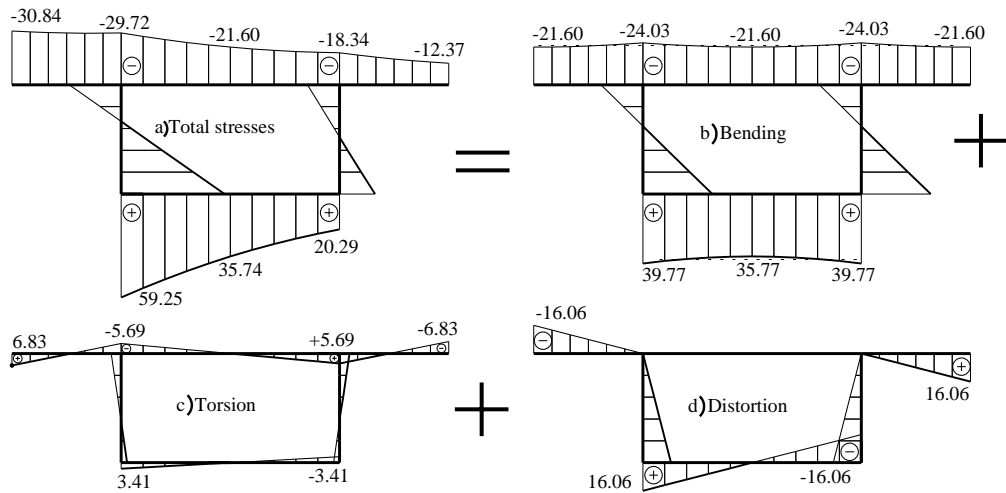


Figure 18: Case 2 Flexion - torsion. *Breakdown of cross-sectional stresses σ_z (N/mm^2) at midspan. a) Total stresses; b) Bending stresses; c) Torsion Stresses; d) Distortion stresses.*

6. CONCLUSIONS

In an earlier study, a unidimensional finite element model had been developed that incorporates all *structural mechanisms* and that may be used for the practical calculation of structures, especially bridge decks. The results of the finite element model had been verified through a comparison with the results of shell-type models. The objective of the present work has been to improve the verification process through a comparison with the experimental results of a real structure, fundamental for its implementation in calculation programs.

A box girder has been tested in the laboratory under two loading states, so that all failure modes intervene. It has been found that the stress values obtained with the element had some differences in the order of $\pm 5\%$, which is a perfectly acceptable value in civil engineering calculations. We may therefore conclude that the unidimensional finite element model has been validated.

A second objective has been to improve the detail with which the rigidity matrix of the element is formulated, and to provide the necessary properties of a particular section, with the objective of offering results that authors with an interest in the use of the finite element method can reproduce. With the information included in the appendices, we believe that this objective has

1
2
3
4
5
6
7
8
9
10
11
12
13
14
15
16
17
18
19
20
21
22
23
24
25
26
27
28
29
30
31
32
33
34
35
36
37
38
39
40
41
42
43
44
45
46
47
48
49
50
51
52
53
54
55
56
57
58
59
60
61
62
63
64
65

been achieved.

Funding

This work was supported by the Junta de Castilla y León (Spain), provided through research project BU062G19.

APPENDIX A. CROSS-SECTIONAL PROPERTIES

On the method of obtaining deformation modes, consult [4], [1], [2]. In the previous article of the authors, [2], the equations were formulated so that they were valid for sections made with different sorts of material. In the present study, the equations were simplified by eliminating the quotients that appeared between the *Young's modulus*, E , and the *elastic shear modulus*, G , in one part of the section, with respect to the values that are considered reference values, respectively E_o and G_o .

The cross-sectional properties for the section of the Figure (1) are the following integrals (5) in relation to the area, A , of the section:

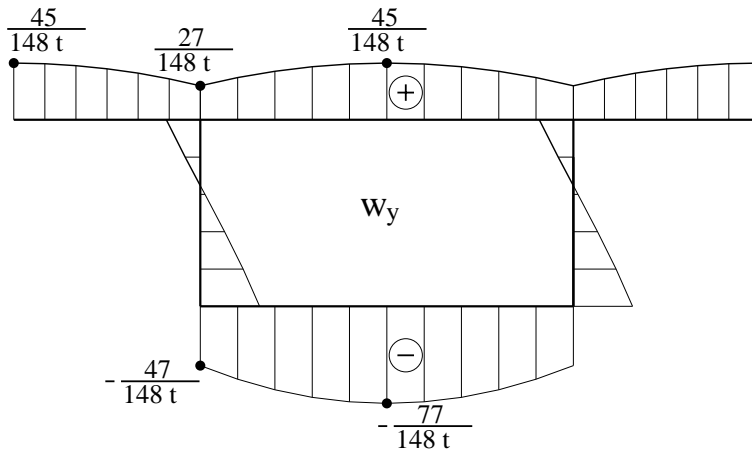
$$\begin{aligned} A &= \int_A dA &= 2 b t \\ I_x &= \int_A y^2 dA &= \frac{37}{1536} b^3 t \\ I_y &= \int_A x^2 dA &= \frac{1}{8} b^3 t \end{aligned} \quad (5)$$

Axial warping displacements related to shear force Q_y represent the longitudinal displacements due to warping, w_y , which is proportional to the occurrence of shear force, Q_y . Shear warping is used to calculate shear stresses ($\tau_{zs} = (Q_y \partial w_y / \partial s)$). See the details in the paper from Jeppe Jönsson [4]. Unlike Jönsson, when the field of displacements is formed, the shear is divided by the cross-section elastic shear modulus, G , so that the warping functions only have dimensions of length.

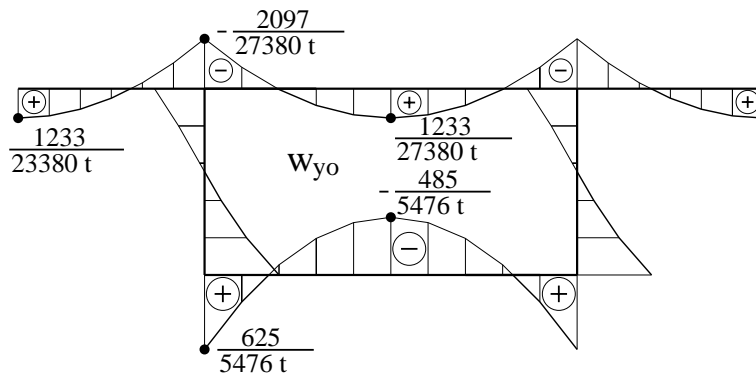
In Figure (19), warping, w_y , due to shear, Q_y , appears, which in this case is the variation in accordance with second-degree polynomials in the upper and lower flange, and with third-degree polynomials in the webs.

As explained in the text, the warping function, w_y , is orthogonalized with regard to the rigid rotation of the section, in order to eliminate the variable, Q_y . To do so, the relation $w_y = C_{yo} \cdot y + w_{yo}$ is established and the condition

1
2
3
4
5
6
7
8
9
10 $\int_A w_{yo} y dA = 0$ is imposed, which yields $C_{yo} = 18912/(6845 b t)$, and finally,
11 the orthogonalized shear warping of the figure (20).
12



13
14
15
16
17
18
19
20
21
22
23
24
25
26
27
28
29 Figure 19: warping w_y due to shear force Q_y
30



31
32
33
34
35
36
37
38
39
40
41
42
43
44
45
46 Figure 20: Orthogonalized warping w_{yo} due to shear force Q_y
47

48 With reference to shear force, Q_y , the following integrals (6) are necessary,
49 to form the rigidity matrix, where the unitary vector of direction of each
50 section wall is $(t_x, t_y) = (dx/ds, dy/ds)$ and the distance along the length of
51 a wall is s :
52
53
54
55
56
57
58
59
60
61
62
63
64
65

$$\begin{aligned}
D_{yy} &= \int_A (t_y)^2 dA &= \frac{1}{2} b t \\
I_{w_{yo}.w_{yo}} &= \int_A (w_{yo})^2 dA &= \frac{341041}{70914200} \frac{b}{t} \\
D_{w_{yo}.w_{yo}} &= \int_A \left(\frac{\partial w_{yo}}{\partial s} \right)^2 dA &= \frac{18912}{6845 b t} \left(\frac{18912}{2 \cdot 6845} - 1 \right) \\
D_{w_{yo}.y} &= \int_A \frac{\partial w_{yo}}{\partial s} t_y dA &= \frac{-2611}{6845}
\end{aligned} \tag{6}$$

The area of shear is obtained by matching the deformation energy with the shear-force effort Q_y , see [2]. In this case, the equation (7) is simplified to obtain A_y , as there is an axis of symmetry.

$$\begin{aligned}
D_{w_y.w_y} &= \int_A (w'_y)^2 dA &= \frac{18912}{6845 b t} \\
A_y &= 1/D_{w_y.w_y} &= \frac{6845}{18912} b t
\end{aligned} \tag{7}$$

Axial warping displacement related to shear force, Q_x , is the longitudinal displacement of the warping, w_x , which is proportional to the occurrence of shear force, Q_x . The calculation is similar to the shear in the other direction. In Figure 21, the warping function, w_x that appears is orthogonalized with respect to the flexural rotation, through the expression $w_x = C_{xo} \cdot x + w_{xo}$, imposing the condition $\int_A w_{xo} y dA = 0$, which yields w_{xo} in Figure 22. The necessary properties to form the rigidity matrix are as follows (8):

$$\begin{aligned}
D_{xx} &= \int_A (t_x)^2 dA &= \frac{3}{2} b t \\
I_{w_{xo}.w_{xo}} &= \int_A (w_{xo})^2 dA &= \frac{1}{1050} \frac{b}{t} \\
D_{w_{xo}.w_{xo}} &= \int_A \left(\frac{\partial w_{xo}}{\partial s} \right)^2 dA &= \frac{4}{25 b t} \\
D_{w_{xo}.x} &= \int_A \frac{\partial w_{xo}}{\partial s} t_x dA &= \frac{-1}{5}
\end{aligned} \tag{8}$$

And the shear area, A_x , according to Equation (9).

1
2
3
4
5
6
7
8
9
10
11
12
13
14
15
16
17
18
19
20
21
22
23
24
25
26
27
28
29
30
31
32
33
34
35
36
37
38
39
40
41
42
43
44
45
46
47
48
49
50
51
52
53
54
55
56
57
58
59
60
61
62
63
64
65

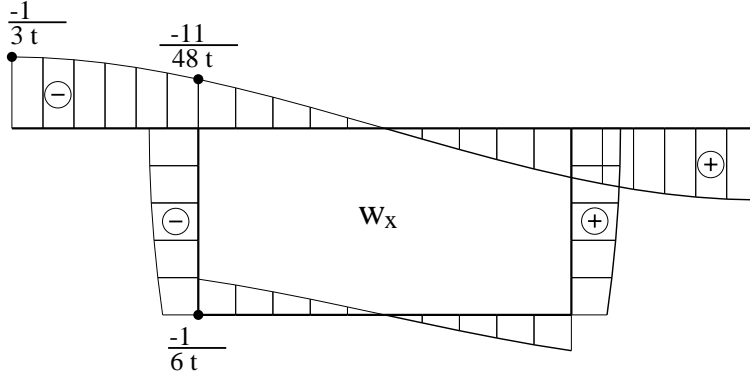


Figure 21: Warping w_x by shear force Q_x

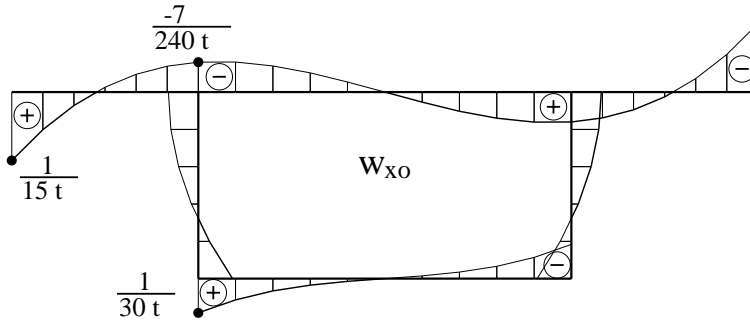


Figure 22: Orthogonalized warping w_{xo} due to shear force Q_x

$$D_{w_x.w_x} = \int_A (w'_x)^2 dA = \frac{4}{5 b t} \quad (9)$$

$$A_x = 1/D_{w_x.w_x} = \frac{5}{4} b t$$

Torsion mode, in which the cross-section is not transversally deformed. Where, w_a represents homogeneous torsional warping shown in Figure (23), which is related to normal stresses due to non-homogeneous torsion, $\sigma_z = E w_a d^2\theta_z/dz^2$.

And, w_{at} is the warping due to shear stress as a result of non-homogeneous torsion, which is related to the following expression: $\tau_{sz} = G \partial w_{at}/\partial s d^3\theta_z/dz^3 = -(S_a/t) \cdot E \cdot d^3\theta_z/dz^3$, see figure (24) where G is the elastic shear modulus.

The following integrals are necessary to include the torsion deformation

1
2
3
4
5
6
7
8
9
10
11
12
13
14
15
16
17
18
19
20
21
22
23
24
25
26
27
28
29
30
31
32
33
34
35
36
37
38
39
40
41
42
43
44
45
46
47
48
49
50
51
52
53
54
55
56
57
58
59
60
61
62
63
64
65

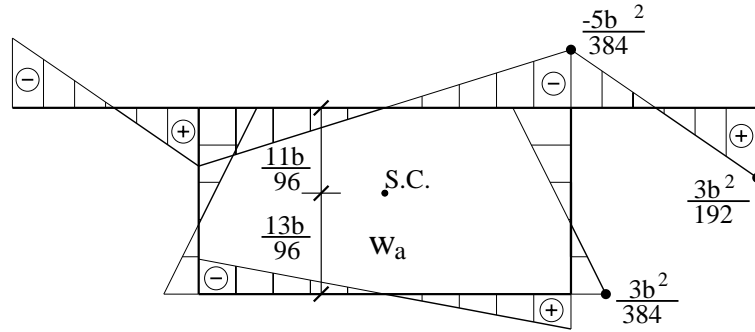


Figure 23: Torsion warping w_a and Shear-Center (S.C.)

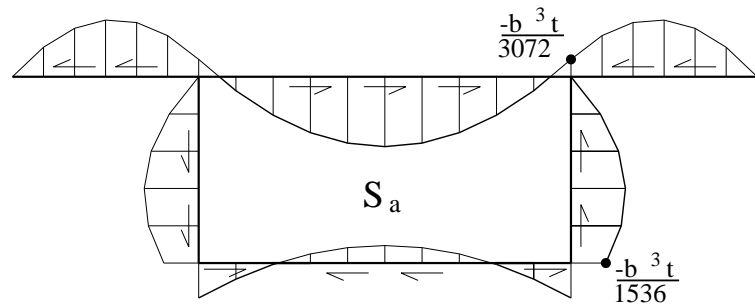


Figure 24: $S_a = -\frac{G}{E} \frac{\partial w_a}{\partial s} \cdot t$ tangential stress due to non-homogeneous torsion.

mode (10) where $h_a = (y - y_a) \cdot t_x - (x - x_a) \cdot t_y$ is the distance from one point to the *shear center* (x_a, y_a) and t_a is an auxiliary variable defined as $t_a = (\partial w_a / \partial s - h_a)$:

$$\begin{aligned}
 I_t &= \int_A (t_a)^2 dA = \frac{b^3 t}{24} \\
 I_a &= \int_A (w_a)^2 dA = \frac{7 b^5 t}{73728}
 \end{aligned}
 \tag{10}$$

Distortion mode. The papers of [5, 6] on obtaining the distortion modes are very interesting, the explanations of which are more detailed than in this paper, due to restrictions on space. In Figure (25), *transversal distortional displacement* (u_{dx}, u_{dy}) is represented, from which the *tangential distortional displacement* given by equation $u_{ds} = u_{dx} \cdot t_x + u_{dy} \cdot t_y$ is shown where (t_x, t_y) is the *unit tangent vector* of the direction of each wall. And in the same way, the

displacement of the wall in a perpendicular direction, $u_{dn} = -u_{dx} \cdot t_y + u_{dy} \cdot t_x$. In the same figure, the scheme of self-balancing forces is shown that the distortion of the section produces.

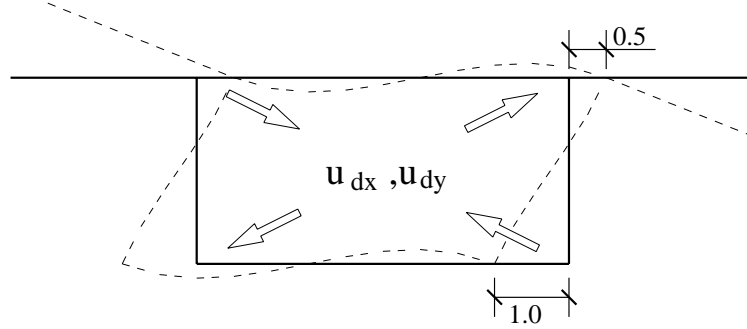


Figure 25: Transversal distortional displacement: (u_{dx}, u_{dy})

The corresponding *warping function*, w_d , can be seen in Figure (26). *Torsion and distortion were very similar and, in the case of distortion, a transversal displacement mode occurred on the cross-sectional plane (u_{dx}, u_{dy}) , according to whether the warping is free or not free, homogeneous and non-homogeneous distortion is obtained.*

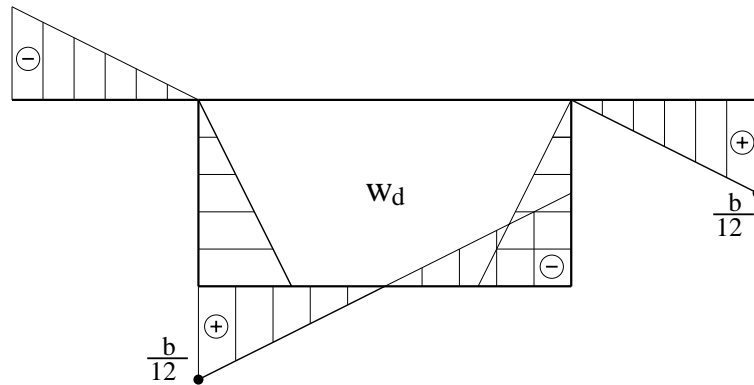


Figure 26: Distortion-related warping w_d

In a similar way to the non-homogeneous torsion, tangential stress appears due to distortion that are represented in Figure (27), which can be obtained with equation $\tau_{sz} = G \partial w_{dt} / \partial s \cdot d^3 \psi_d / dz^3 = (S_d / t) \cdot E \cdot d^3 \psi_d / dz^3$, in which ψ_d is the intensity of the distortion throughout the girder.

1
2
3
4
5
6
7
8
9
10
11
12
13
14
15
16
17
18
19
20
21
22
23
24
25
26
27
28
29
30
31
32
33
34
35
36
37
38
39
40
41
42
43
44
45
46
47
48
49
50
51
52
53
54
55
56
57
58
59
60
61
62
63
64
65

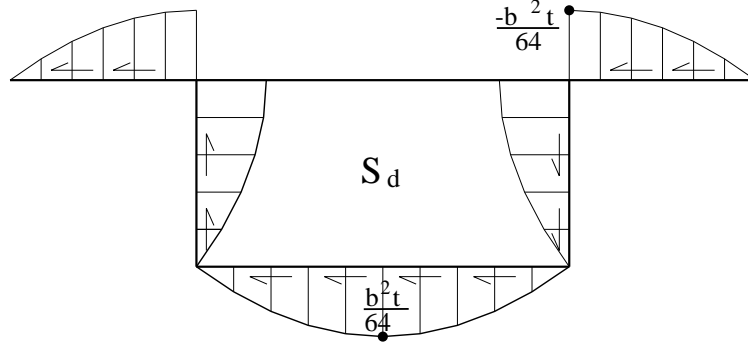


Figure 27: $S_d = \frac{G}{E} \frac{\partial w_{dt}}{\partial s} \cdot t$ tangential stress due to non-homogeneous distortion.

The necessary constants for the distortion mode are as follows (11).

$$\begin{aligned}
 K_d &= \int \frac{t^3}{12} \cdot \left(\frac{du_{dn}}{ds} \right)^2 ds = 96 \frac{t^3}{b^3} \\
 I_d &= \int_A (w_d)^2 dA = \frac{b^3 t}{128}
 \end{aligned} \tag{11}$$

When obtaining the deformation modes, some are orthogonalized with others to remove any coupling between them. Despite this process, the torsion and distortion modes were coupled by the tangential stresses that appeared in closed parts of the sections, in which (12) details the constants that coupled those modes. In them, $t_d = (u_{ds} - \partial w_d / \partial s)$.

$$\begin{aligned}
 D_{t_d \cdot t_d} &= \int_A (t_d)^2 dA = \frac{3}{8} b t \\
 D_{t_d \cdot t_a} &= \int_A t_a t_d dA = \frac{-b t}{8}
 \end{aligned} \tag{12}$$

APPENDIX B. ELEMENT STIFFNESS MATRIX

In this appendice, the definition of the rigidity matrix is shown for the finite unidimensional element with three nodes from Figure (28), in which the *shape functions* are from Figure (29).

Denoting with the following sign, (t) , the derivatives of the form functions with respect to the z coordinate, and striking out the terms that are

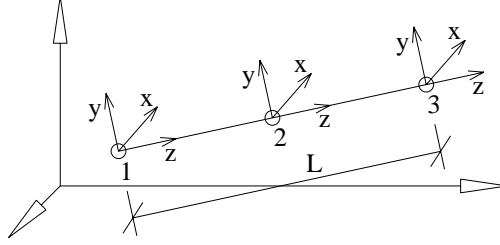
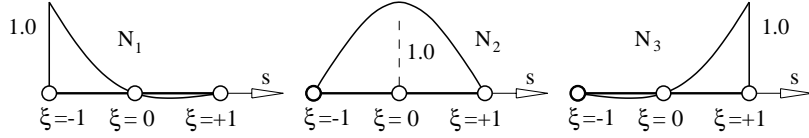


Figure 28: Geometric definition of the element.

CONTINUITY C0

DOF: $u_x, u_y, u_z, \theta_x, \theta_y, \chi_x, \chi_y$



CONTINUITY C1

DOF: $\theta_z, \theta'_z, \Psi_d, \Psi'_d$

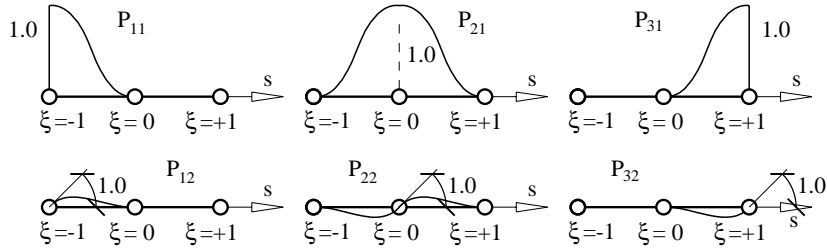


Figure 29: Shape Functions.

discounted, the rigidity submatrix, $[k_{ij}]$, is as follows:

$$[k_{ij}] = \int_0^L \begin{bmatrix} K_{0,0} & \cancel{K_{0,1}} & 0 & \cancel{K_{0,3}} & K_{0,4} & 0 & 0 & K_{0,7} & \cancel{K_{0,8}} & 0 & 0 \\ \cancel{K_{1,0}} & K_{1,1} & 0 & K_{1,3} & \cancel{K_{1,4}} & 0 & 0 & \cancel{K_{1,7}} & K_{1,8} & 0 & 0 \\ 0 & 0 & K_{2,2} & 0 & 0 & 0 & 0 & 0 & 0 & 0 & 0 \\ \cancel{K_{3,0}} & K_{3,1} & 0 & K_{3,3} & \cancel{K_{3,4}} & 0 & 0 & \cancel{K_{3,7}} & K_{3,8} & 0 & 0 \\ K_{4,0} & \cancel{K_{4,1}} & 0 & \cancel{K_{4,3}} & K_{4,4} & 0 & 0 & K_{4,7} & \cancel{K_{4,8}} & 0 & 0 \\ 0 & 0 & 0 & 0 & 0 & K_{5,5} & K_{5,6} & 0 & 0 & K_{5,9} & K_{5,10} \\ 0 & 0 & 0 & 0 & 0 & K_{6,5} & K_{6,6} & 0 & 0 & K_{6,9} & K_{6,10} \\ K_{7,0} & \cancel{K_{7,1}} & 0 & \cancel{K_{7,3}} & K_{7,4} & 0 & 0 & K_{7,7} & \cancel{K_{7,8}} & 0 & 0 \\ \cancel{K_{8,0}} & K_{8,1} & 0 & K_{8,3} & \cancel{K_{8,4}} & 0 & 0 & \cancel{K_{8,7}} & K_{8,8} & 0 & 0 \\ 0 & 0 & 0 & 0 & 0 & K_{9,5} & K_{9,6} & 0 & 0 & K_{9,9} & K_{9,10} \\ 0 & 0 & 0 & 0 & 0 & K_{10,5} & K_{10,6} & 0 & 0 & K_{10,9} & K_{10,10} \end{bmatrix} dz$$

Axial force.

$$K_{2.2} = N'_i E_o A N'_j$$

Flexion on the x-z plane. The orthogonalization of shear warping with regard to rotation means that $I_{w_{x_o}.x} = 0$, for which reason it is discounted.

$$\begin{aligned}
K_{4.4} &= \frac{N'_i E_o I_y N'_j}{\cancel{N'_i E_o A_x I_{w_{x_o}.x} N'_j}} + N_i G_o D_{xx} N_j \\
K_{4.7} &= - \frac{N'_i E_o A_x \cancel{I_{w_{x_o}.x} N'_j}}{\cancel{N'_i E_o A_x I_{w_{x_o}.x} N'_j}} - N_i G_o A_x D_{w_{x_o}.x} N_j \\
K_{7.4} &= - \frac{N'_i E_o A_x \cancel{I_{w_{x_o}.x} N'_j}}{\cancel{N'_i E_o A_x I_{w_{x_o}.x} N'_j}} - N_i G_o A_x D_{w_{x_o}.x} N_j \\
K_{7.7} &= \frac{N'_i E_o A_x^2 I_{w_{x_o}.w_{x_o}} N'_j}{\cancel{N'_i E_o A_x I_{w_{x_o}.x} N'_j}} + N_i G_o A_x^2 D_{w_{x_o}.w_{x_o}} N_j \\
K_{0.0} &= N'_i G_o D_{xx} N'_j \\
K_{0.4} &= - N'_i G_o D_{xx} N_j \\
K_{4.0} &= - N_i G_o D_{xx} N'_j \\
K_{0.7} &= N'_i G_o A_x D_{w_{x_o}.x} N_j \\
K_{7.0} &= N_i G_o A_x D_{w_{x_o}.x} N'_j
\end{aligned}$$

Flexion on the y-z plane. The orthogonalization of shear warping with regard to rotation means that $I_{w_{y_o}.y} = 0$, for which reason it is discounted.

$$\begin{aligned}
K_{3.3} &= N'_i E_o I_x N'_j + N_i G_o D_{yy} N_j \\
K_{3.8} &= \frac{N'_i E_o A_y \cancel{I_{w_{y_o}.y} N'_j}}{\cancel{N'_i E_o A_y I_{w_{y_o}.y} N'_j}} + N_i G_o A_y D_{w_{y_o}.y} N_j \\
K_{8.3} &= \frac{N'_i E_o A_y \cancel{I_{w_{y_o}.y} N'_j}}{\cancel{N'_i E_o A_y I_{w_{y_o}.y} N'_j}} + N_i G_o A_y D_{w_{y_o}.y} N_j \\
K_{8.8} &= \frac{N'_i E_o A_y^2 I_{w_{y_o}.w_{y_o}} N'_j}{\cancel{N'_i E_o A_y I_{w_{y_o}.y} N'_j}} + N_i G_o A_y^2 D_{w_{y_o}.w_{y_o}} N_j \\
K_{1.1} &= N'_i G_o D_{yy} N'_j \\
K_{1.3} &= N'_i G_o D_{yy} N_j \\
K_{3.1} &= N_i G_o D_{yy} N'_j \\
K_{1.8} &= N'_i G_o A_y D_{w_{y_o}.y} N_j \\
K_{8.1} &= N_i G_o A_y D_{w_{y_o}.y} N'_j
\end{aligned}$$

Couping between flexions. The following are all discounted, because their inclusion in no provides better results.

$$\begin{aligned}
K_{3.7} &= \frac{N'_i E_o A_x \cancel{I_{w_{x_o}.y} N'_j}}{\cancel{N'_i E_o A_x I_{w_{x_o}.y} N'_j}} + \frac{N_i G_o A_x \cancel{D_{w_{x_o}.y} N_j}}{\cancel{N_i G_o A_x D_{w_{x_o}.y} N_j}} \\
K_{4.8} &= - \frac{N'_i E_o A_y \cancel{I_{w_{y_o}.x} N'_j}}{\cancel{N'_i E_o A_y I_{w_{y_o}.x} N'_j}} - \frac{N_i G_o A_y \cancel{D_{w_{y_o}.x} N_j}}{\cancel{N_i G_o A_y D_{w_{y_o}.x} N_j}} \\
K_{7.3} &= \frac{N'_i E_o A_x \cancel{I_{w_{x_o}.y} N'_j}}{\cancel{N'_i E_o A_x I_{w_{x_o}.y} N'_j}} + \frac{N_i G_o A_x \cancel{D_{w_{x_o}.y} N_j}}{\cancel{N_i G_o A_x D_{w_{x_o}.y} N_j}} \\
K_{8.4} &= - \frac{N'_i E_o A_y \cancel{I_{w_{y_o}.x} N'_j}}{\cancel{N'_i E_o A_y I_{w_{y_o}.x} N'_j}} - \frac{N_i G_o A_y \cancel{D_{w_{y_o}.x} N_j}}{\cancel{N_i G_o A_y D_{w_{y_o}.x} N_j}} \\
K_{7.8} &= \frac{N'_i E_o A_x A_y \cancel{I_{w_{y_o}.w_{x_o}} N'_j}}{\cancel{N'_i E_o A_x A_y I_{w_{y_o}.w_{x_o}} N'_j}} + \frac{N_i G_o A_x A_y \cancel{D_{w_{y_o}.w_{x_o}} N_j}}{\cancel{N_i G_o A_x A_y D_{w_{y_o}.w_{x_o}} N_j}} \\
K_{8.7} &= \frac{N'_i E_o A_x A_y \cancel{I_{w_{y_o}.w_{x_o}} N'_j}}{\cancel{N'_i E_o A_x A_y I_{w_{y_o}.w_{x_o}} N'_j}} + \frac{N_i G_o A_x A_y \cancel{D_{w_{y_o}.w_{x_o}} N_j}}{\cancel{N_i G_o A_x A_y D_{w_{y_o}.w_{x_o}} N_j}}
\end{aligned}$$

$$\begin{aligned}
K_{0.1} &= \cancel{N'_i G_o D_{xy} N'_j} \\
K_{1.0} &= \cancel{N'_i G_o D_{xy} N'_j} \\
K_{3.4} &= - \cancel{N_i G_o D_{xy} N_j} \\
K_{4.3} &= - \cancel{N_i G_o D_{xy} N_j} \\
K_{0.3} &= \cancel{N'_i G_o D_{xy} N'_j} \\
K_{1.4} &= - \cancel{N'_i G_o D_{xy} N'_j} \\
K_{3.0} &= \cancel{N_i G_o D_{xy} N_j} \\
K_{4.1} &= - \cancel{N_i G_o D_{xy} N_j} \\
K_{0.8} &= \cancel{N'_i G_o A_y D_{w_{y o}, x} N'_j} \\
K_{1.7} &= \cancel{N'_i G_o A_x D_{w_{x o}, y} N'_j} \\
K_{7.1} &= \cancel{N_i G_o A_x D_{w_{x o}, y} N_j} \\
K_{8.0} &= \cancel{N_i G_o A_y D_{w_{y o}, x} N_j}
\end{aligned}$$

Torsion - distortions. The orthogonalization between torsion and distortion warping means that $I_{w_a, w_d} = 0$, for which reason the terms in which it appears are discounted.

$$\begin{aligned}
K_{5.5} &= P''_{i1} E_o I_a P''_{j1} + P'_{i1} G_o I_t P'_{j1} \\
K_{5.6} &= P''_{i1} E_o I_a P''_{j2} + P'_{i1} G_o I_t P'_{j2} \\
K_{6.5} &= P''_{i2} E_o I_a P''_{j1} + P'_{i2} G_o I_t P'_{j1} \\
K_{6.6} &= P''_{i2} E_o I_a P''_{j2} + P'_{i2} G_o I_t P'_{j2} \\
K_{5.9} &= - \cancel{P''_{i1} E_o I_{w_a, w_d} P''_{j1}} + P'_{i1} G_o D_{t_d, t_a} P'_{j1} \\
K_{5.10} &= - \cancel{P''_{i1} E_o I_{w_a, w_d} P''_{j2}} + P'_{i1} G_o D_{t_d, t_a} P'_{j2} \\
K_{6.9} &= - \cancel{P''_{i2} E_o I_{w_a, w_d} P''_{j1}} + P'_{i2} G_o D_{t_d, t_a} P'_{j1} \\
K_{6.10} &= - \cancel{P''_{i2} E_o I_{w_a, w_d} P''_{j2}} + P'_{i2} G_o D_{t_d, t_a} P'_{j2} \\
K_{9.5} &= - \cancel{P''_{i1} E_o I_{w_a, w_d} P''_{j1}} + P'_{i1} G_o D_{t_d, t_a} P'_{j1} \\
K_{9.6} &= - \cancel{P''_{i1} E_o I_{w_a, w_d} P''_{j2}} + P'_{i1} G_o D_{t_d, t_a} P'_{j2} \\
K_{10.5} &= - \cancel{P''_{i2} E_o I_{w_a, w_d} P''_{j1}} + P'_{i2} G_o D_{t_d, t_a} P'_{j1} \\
K_{10.6} &= - \cancel{P''_{i2} E_o I_{w_a, w_d} P''_{j2}} + P'_{i2} G_o D_{t_d, t_a} P'_{j2} \\
K_{9.9} &= P''_{i1} E_o I_d P''_{j1} + P'_{i1} G_o D_{t_d, t_d} P'_{j1} + P_{i1} E_o K_d P_{j1} \\
K_{9.10} &= P''_{i1} E_o I_d P''_{j2} + P'_{i1} G_o D_{t_d, t_d} P'_{j2} + P_{i1} E_o K_d P_{j2} \\
K_{10.9} &= P''_{i2} E_o I_d P''_{j1} + P'_{i2} G_o D_{t_d, t_d} P'_{j1} + P_{i2} E_o K_d P_{j1} \\
K_{10.10} &= P''_{i2} E_o I_d P''_{j2} + P'_{i2} G_o D_{t_d, t_d} P'_{j2} + P_{i2} E_o K_d P_{j2}
\end{aligned}$$

APPENDIX C. NOTATION

The notation used to represent the variables is provided below:

1
2
3
4
5
6
7
8
9
10
11
12
13
14
15
16
17
18
19
20
21
22
23
24
25
26
27
28
29
30
31
32
33
34
35
36
37
38
39
40
41
42
43
44
45
46
47
48
49
50
51
52
53
54
55
56
57
58
59
60
61
62
63
64
65

	Notation	Units
Longitudinal coordinate	z	m
Coordinates of the cross-section	x, y	m
Elastic center	$x_c = 0, y_c = 0$	m
Shear center	x_a, y_a	m
Unit tangent vector	t_x, t_y	—
Area of cross-section	A	m^2
Moments of inertia	I_x, I_y	m^4
Reference Young's modulus	E_o	kN/m^2
Reference elastic shear modulus	G_o	kN/m^2
Total transverse displacement of any point	$v_x(x, y, z), v_y(x, y, z)$	m
Transverse displacement of the shear center	$u_x(z), u_y(z)$	m
Total longitudinal displacement of any point	$v_z(x, y, z)$	m
Longitudinal displacement of the elastic center	$u_z(z)$	m
Shear areas	A_x, A_y, A_{xy}	m^2
Warping due to shear forces	$w_x(x, y), w_y(x, y)$	m^{-1}
Torsion constant	I_t	m^4
Warping torsion constant	I_a	m^6
Intensity of rotation	$\theta_z(z)$	—
St. Venant torsional moment	$M_{zu} = G_o I_t \theta'_z$	$kN m$
Torsional warping moment	$M_{zw} = -E_o I_a \theta'''_z$	$kN m$
Torsional bimoment	$B_w = E_o I_a \theta''_z$	$kN m^2$
St. Venant torsional warping around the shear center	$w_a(x, y)$	m^2
Warping induced by the non homogeneous torsional shear stress (neglected)	$w_{at}(x, y)$	m^4
Distortion constant	D_{t_d, t_d}	m^4
Warping distortion constant	I_d	m^6
Distortional bending constant	K_d	m^2
Torsional-distortional constant	D_{t_a, t_d}	m^2
Intensity of distortion	$\psi_d(z)$	—
Distortional moment	$M_{du} = -G_o D_{t_d, t_d} \psi'_d$	$kN m$
Distortional warping moment	$M_{dw} = E_o I_d \psi'''_d$	$kN m$
Distortional bimoment	$B_d = -E_o I_d \psi''_d$	$kN m^2$
Distortional warping	$w_d(x, y)$	m^2
Warping induced by the non-homogeneous distortional shear stress (neglected)	$w_{dt}(x, y)$	m^4
In plane distortional displacement mode	$u_{dx}(x, y), u_{dy}(x, y)$	m
Tangential distortional displacement	u_{ds}	m

1
2
3
4
5
6
7
8
9 **REFERENCES**

10
11 **References**

- 12
13 [1] Cambronero-Barrientos, F., 2013. Análisis conjunto de los modos re-
14 sistentes en secciones de paredes delgadas y su aplicación a tableros de
15 puente. Ph.D. thesis. University of Cantabria. Santander, Spain. URL:
16 <http://hdl.handle.net/10902/2311>.
17
18 [2] Cambronero-Barrientos, F., Díaz-del Valle, J., Martínez-Martínez,
19 J.A., 2017. Beam element for thin-walled beams with torsion, dis-
20 tortion, and shear lag. *Engineering Structures* 143, 571–588. URL:
21 <https://www.sciencedirect.com/science/article/abs/pii/S0141029617312282>,
22 doi:<https://doi.org/10.1016/j.engstruct.2017.04.020>.
23
24 [3] Guo, Z., Li, L., Zhang, J., 2019. Theoretical analysis for shear-
25 lag effect of variable box section cantilever girder based on bar
26 simulation method. *China Civil Engineering Journal* 52. URL:
27 http://manu36.magtech.com.cn/Jwk_tmgcxb/CN/Y2019/V52/I8/72.
28
29 [4] Jönsson, J., 1998. Determination of shear stresses, warping
30 functions and section properties of thin-walled beams using fi-
31 nite elements. *Computers & Structures* 68, 393–410. URL:
32 <http://www.sciencedirect.com/science/article/pii/S0045794998000704>,
33 doi:10.1016/S0045-7949(98)00070-4.
34
35 [5] Jönsson, J., 1999a. Distortional theory of thin-walled
36 beams. *Thin-Walled Structures* 33, 269 – 303. URL:
37 <http://www.sciencedirect.com/science/article/pii/S0263823198000500>,
38 doi:[http://dx.doi.org/10.1016/S0263-8231\(98\)00050-0](http://dx.doi.org/10.1016/S0263-8231(98)00050-0).
39
40 [6] Jönsson, J., 1999b. Distortional warping functions and shear distribu-
41 tions in thin-walled beams. *Thin-Walled Structures* 33, 245 – 268. URL:
42 <http://www.sciencedirect.com/science/article/pii/S0263823198000482>,
43 doi:[http://dx.doi.org/10.1016/S0263-8231\(98\)00048-2](http://dx.doi.org/10.1016/S0263-8231(98)00048-2).
44
45 [7] Li, X., Wan, S., Shen, K., Zhou, P., 2020. Finite beam
46 element with exact shape functions for torsional analy-
47 sis in thin-walled single- or multi-cell box girders. *Jour-
48 nal of Constructional Steel Research* 172, 106189. URL:
49
50
51
52
53
54
55
56
57
58
59
60
61
62
63
64
65

1
2
3
4
5
6
7
8
9
10 <https://www.sciencedirect.com/science/article/pii/S0143974X20307410>,
11 [doi:https://doi.org/10.1016/j.jcsr.2020.106189](https://doi.org/10.1016/j.jcsr.2020.106189).

12 [8] Li, X., Wan, S., Zhang, Y., Zhou, M., Mo, Y., 2021. Beam fi-
13 nite element for thin-walled box girders considering shear lag and
14 shear deformation effects. *Engineering Structures* 233, 111867. URL:
15 <https://www.sciencedirect.com/science/article/pii/S0141029621000171>,
16 [doi:https://doi.org/10.1016/j.engstruct.2021.111867](https://doi.org/10.1016/j.engstruct.2021.111867).

17
18
19
20 [9] Luo, Z., Yuan, H., , Niu, X., 2019. A new approach for
21 free vibration analysis of thin-walled box girder consider-
22 ing shear lag effect. *Advances in Civil Engineering* 2019.
23 URL: <https://www.hindawi.com/journals/ace/2019/3902828/>,
24 [doi:https://doi.org/10.1155/2019/3902828](https://doi.org/10.1155/2019/3902828).

25
26
27 [10] Pan, D.G., Fu, X.Q., Wei, S.S., Chen, F., Yang, S.P., 2018.
28 Semi-analytic solution for shear lag effect of cantilever box
29 girders with varying depth. *Engineering Mechanics* 35. URL:
30 <http://engineeringmechanics.cn/article/doi/10.6052/j.issn.1000-4750.2017.08>
31 [doi:http://dx.doi.org/10.6052/j.issn.1000-4750.2017.08.0643](http://dx.doi.org/10.6052/j.issn.1000-4750.2017.08.0643).

32
33
34 [11] Tan, M., Cheng, W., 2019. Non-linear lateral buckling
35 analysis of unequal thickness thin-walled box beam un-
36 der an eccentric load. *Thin-Walled Structures* 139. URL:
37 <https://www.sciencedirect.com/science/article/abs/pii/S026382311831187X>,
38 [doi:https://doi.org/10.1016/j.tws.2019.02.028](https://doi.org/10.1016/j.tws.2019.02.028).

39
40
41 [12] Tan, M., Cheng, W., 2020. Nonlinear buckling anal-
42 ysis of thin-walled box beams considering shear lag.
43 *Mathematical Problems in Engineering* 2020. URL:
44 <https://www.hindawi.com/journals/mpe/2020/3198410/>,
45 [doi:https://doi.org/10.1155/2020/3198410](https://doi.org/10.1155/2020/3198410).


46
47
48 [13] Tsipitsis, I.N., Sapountzaki, O.E., 2020. Analysis of compos-
49 ite bridges with intermediate diaphragms & assessment of de-
50 sign guidelines. *Computers & Structures* 234, 106252. URL:
51 <http://www.sciencedirect.com/science/article/pii/S0045794920300559>,
52 [doi:https://doi.org/10.1016/j.compstruc.2020.106252](https://doi.org/10.1016/j.compstruc.2020.106252).

- 1
2
3
4
5
6
7
8
9
10
11
12
13
14
15
16
17
18
19
20
21
22
23
24
25
26
27
28
29
30
31
32
33
34
35
36
37
38
39
40
41
42
43
44
45
46
47
48
49
50
51
52
53
54
55
56
57
58
59
60
61
62
63
64
65
- [14] Tsipstsis, I.N., Sapountzakis, E.J., 2017. Generalized warping and distortional analysis of curved beams with isogeometric methods. *Computers & Structures* 191, 33 – 50. URL: <http://www.sciencedirect.com/science/article/pii/S0045794917302006>, doi:<https://doi.org/10.1016/j.compstruc.2017.06.007>.
- [15] Wen, Y., lin Chen, Z., 2020. One-dimensional finite element analysis of warping torsion for thin-walled members with open-closed cross sections based on compatible warping field. *Engineering Mechanics* 37. URL: <http://engineeringmechanics.cn/cn/article/doi/10.6052/j.issn.1000-4750.2019>
- [16] Zhang, L., Ji, A., Zhu, W., 2019. A novel approach to perform the identification of cross-section deformation modes for thin-walled structures in the framework of a higher order beam theory. *Applied Sciences* 9. URL: <https://www.mdpi.com/2076-3417/9/23/5186>, doi:<https://doi.org/10.3390/app9235186>.
- [17] Zhang, L., Ji, A., Zhu, W., Peng, L., 2018. On the identification of sectional deformation modes of thin-walled structures with doubly symmetric cross-sections based on the shell-like deformation. *Symmetry* 10. URL: <https://www.mdpi.com/2073-8994/10/12/759>, doi:<https://doi.org/10.3390/sym10120759>.
- [18] Zhang, L., Zhu, W., Ji, A., 2019. Application of pattern recognition to the identification of cross-section deformation modes of thin-walled structures. *IEEE Access* 7, 169586–169598. URL: <https://ieeexplore.ieee.org/document/8907882>, doi:<https://doi.org/10.1109/ACCESS.2019.2954712>.



Click here to access/download
LaTeX Source File
References.bib

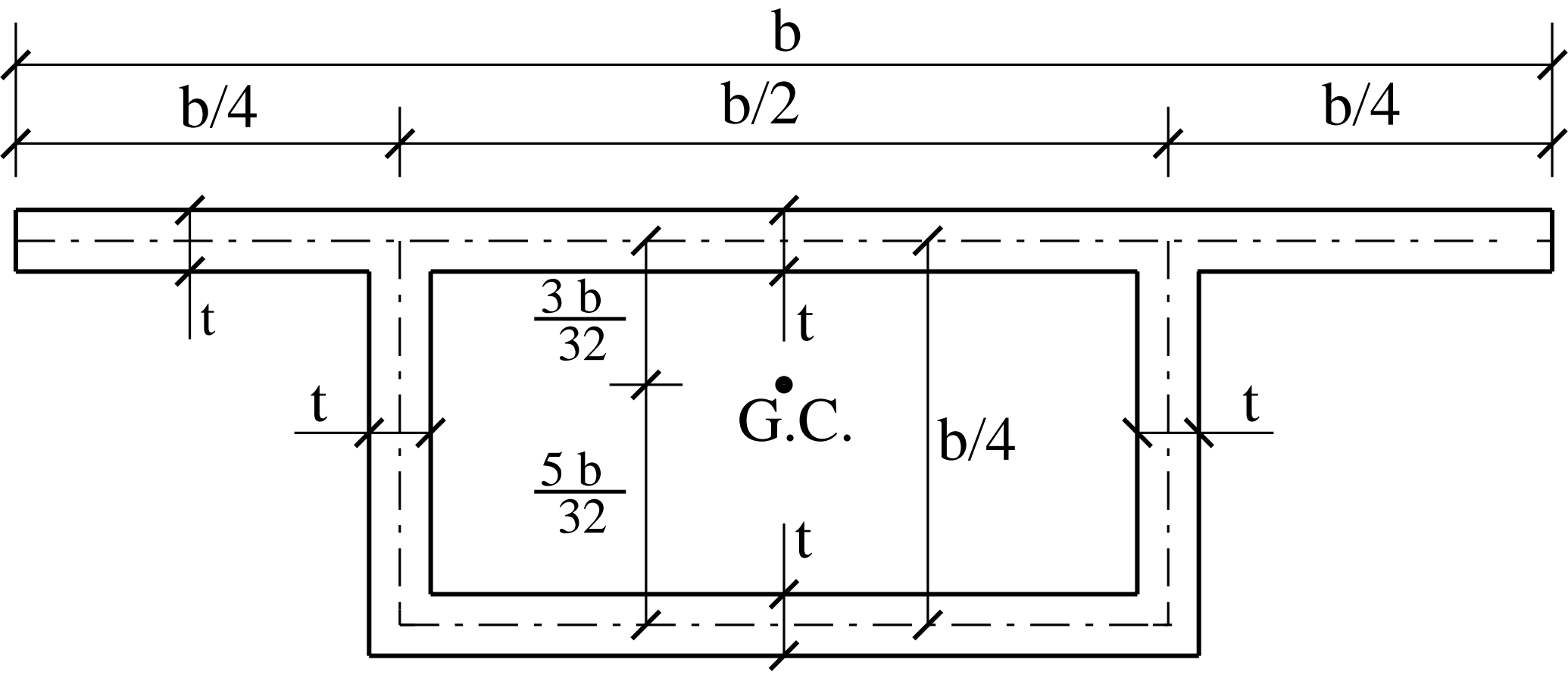


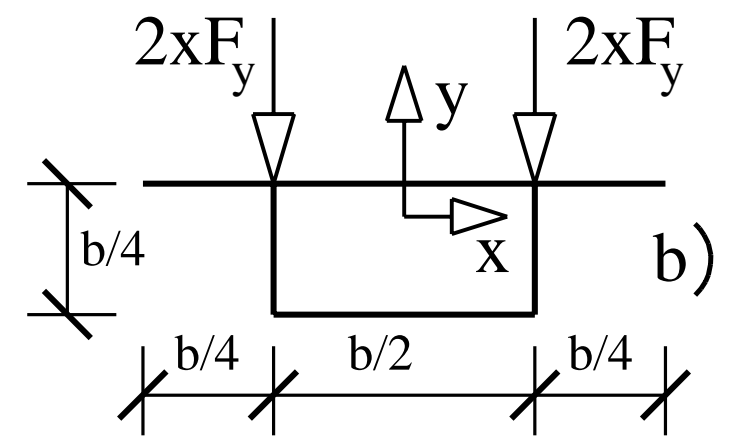
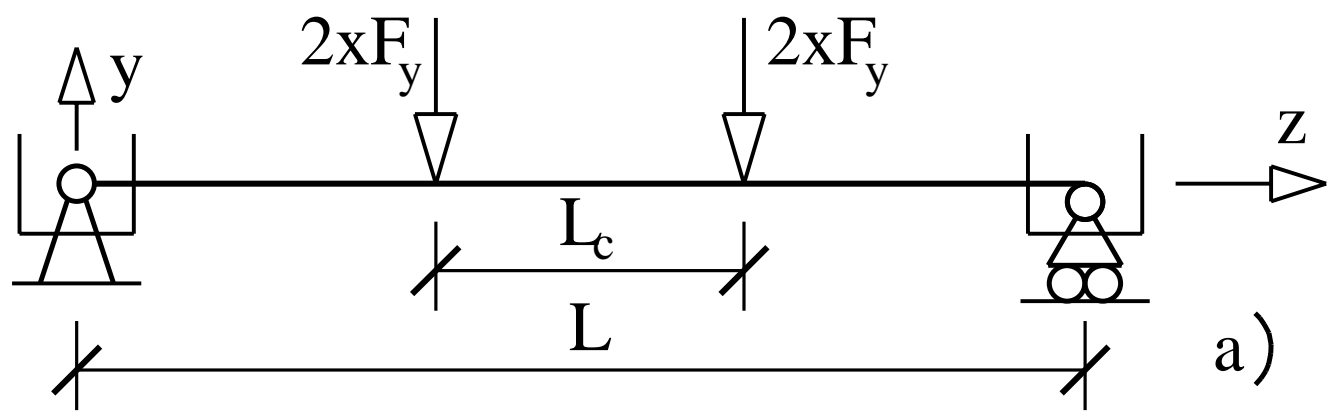


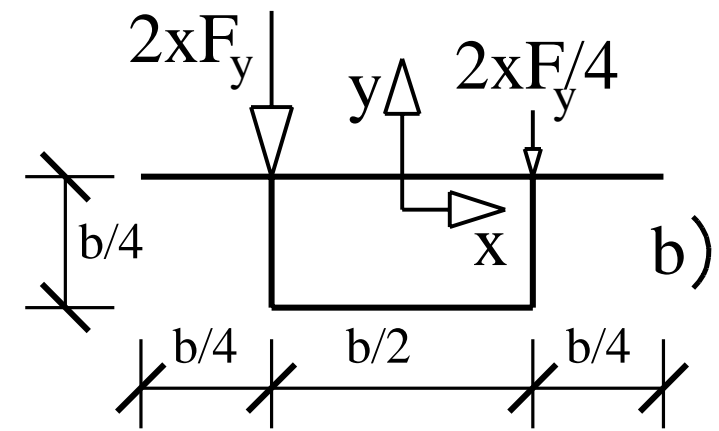
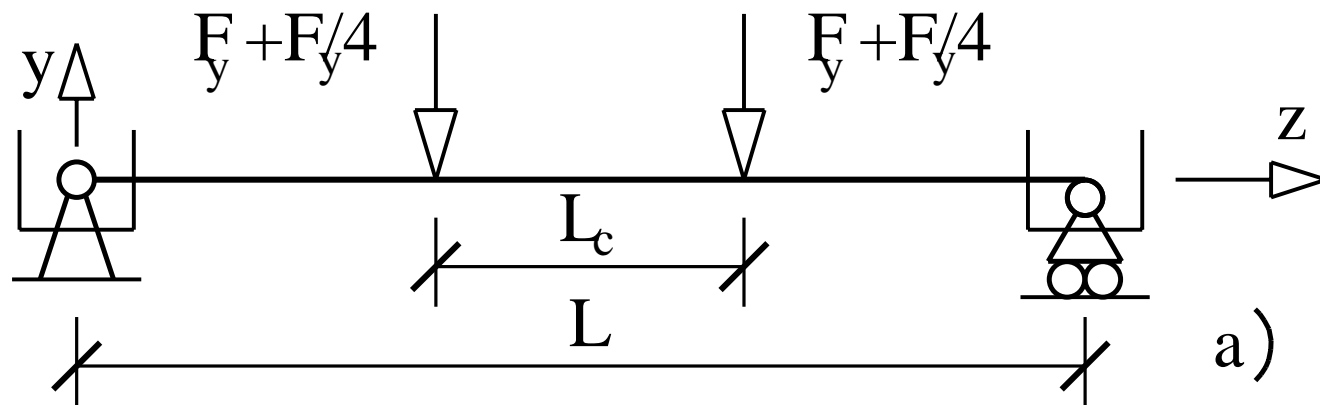
Click here to access/download

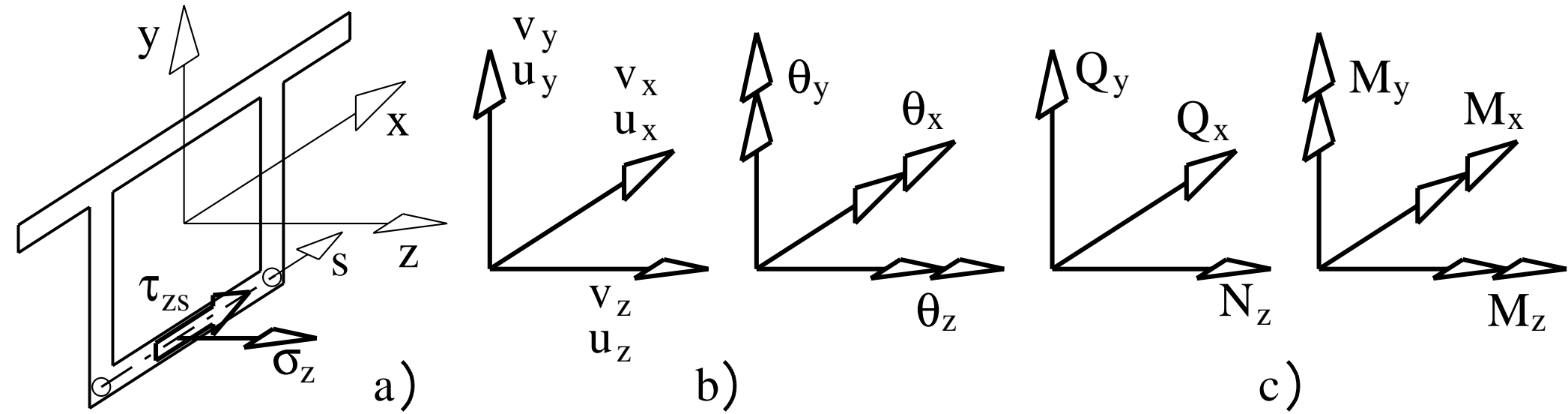
LaTeX Source File

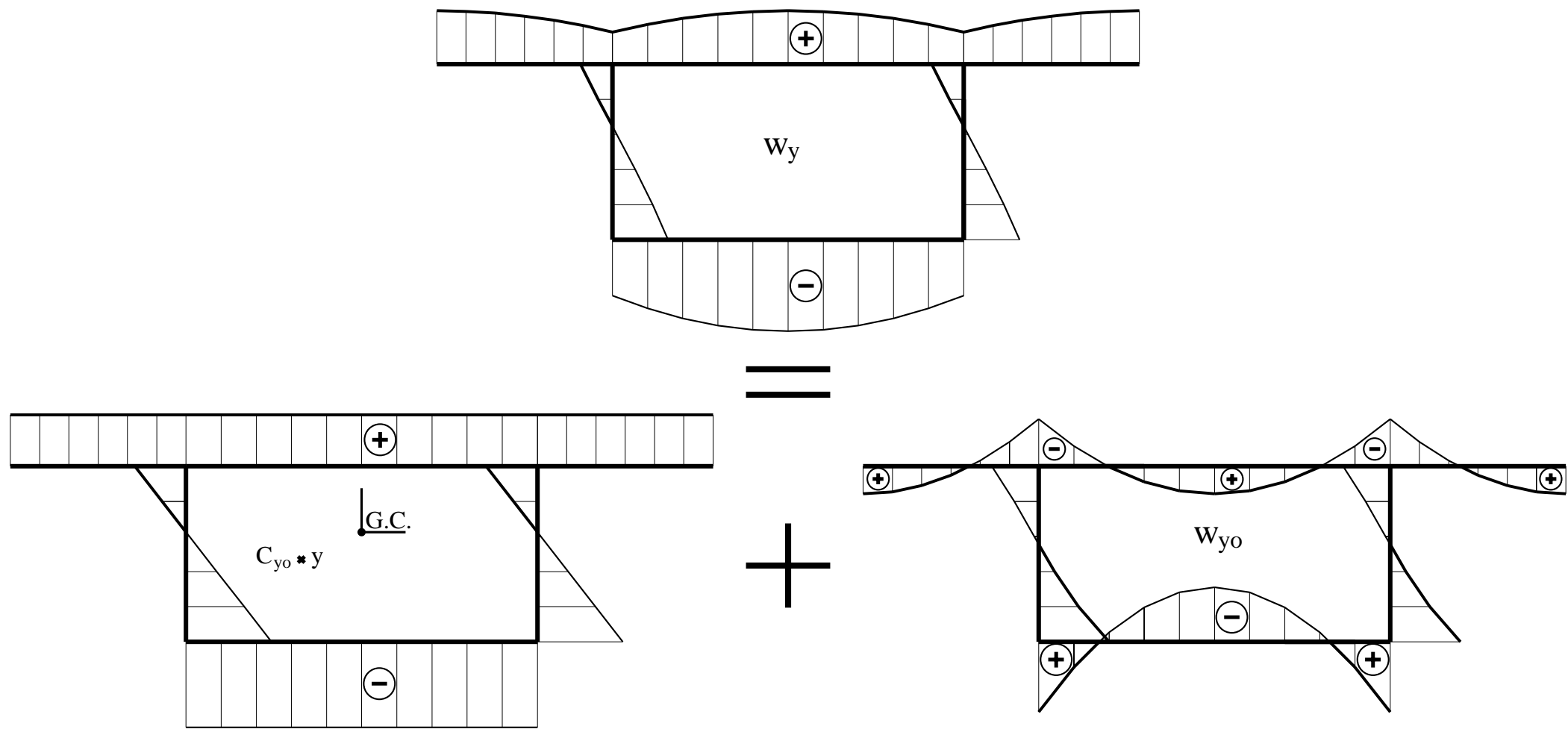
Experimental_verification_of_Beam_element_for_thin_w
alled.tex

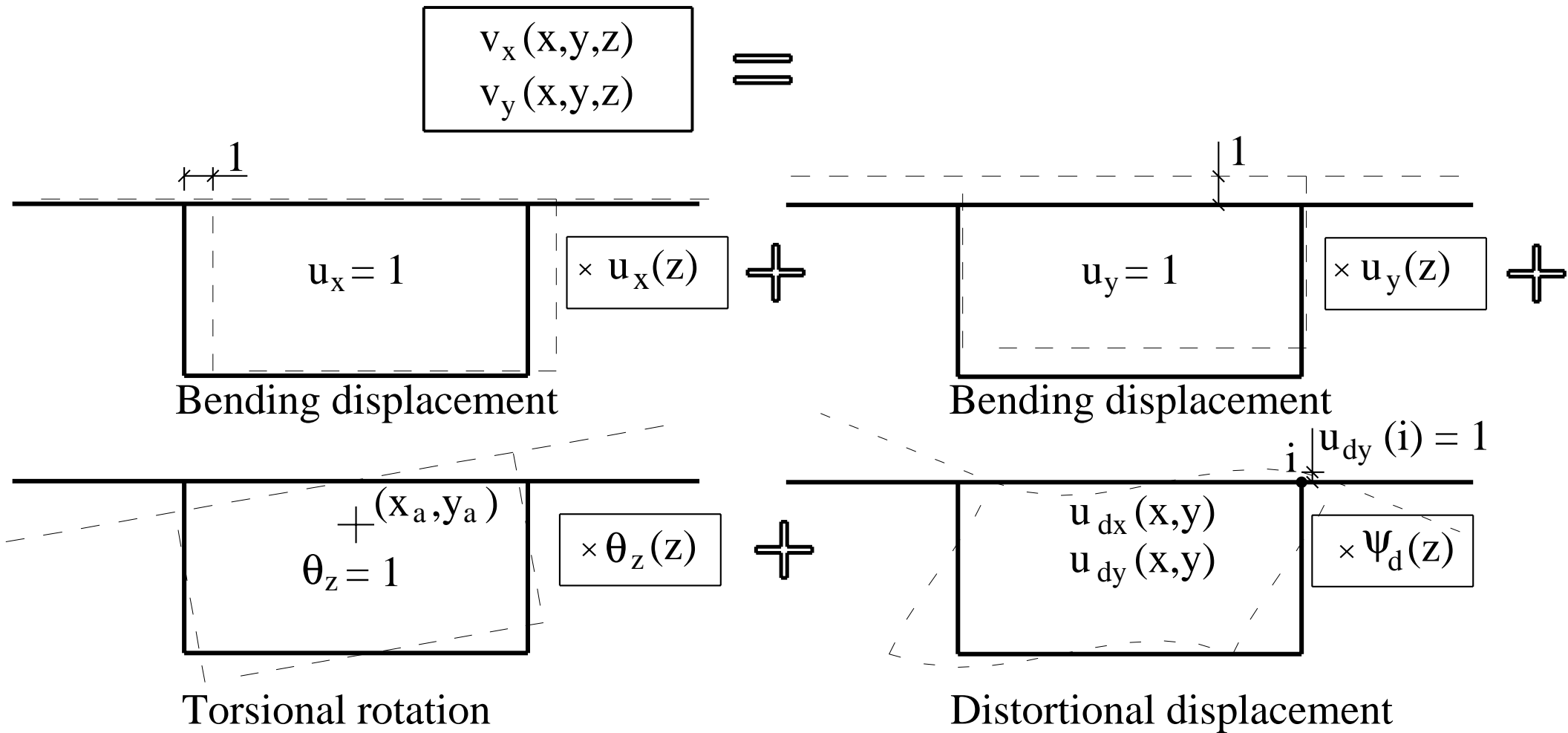


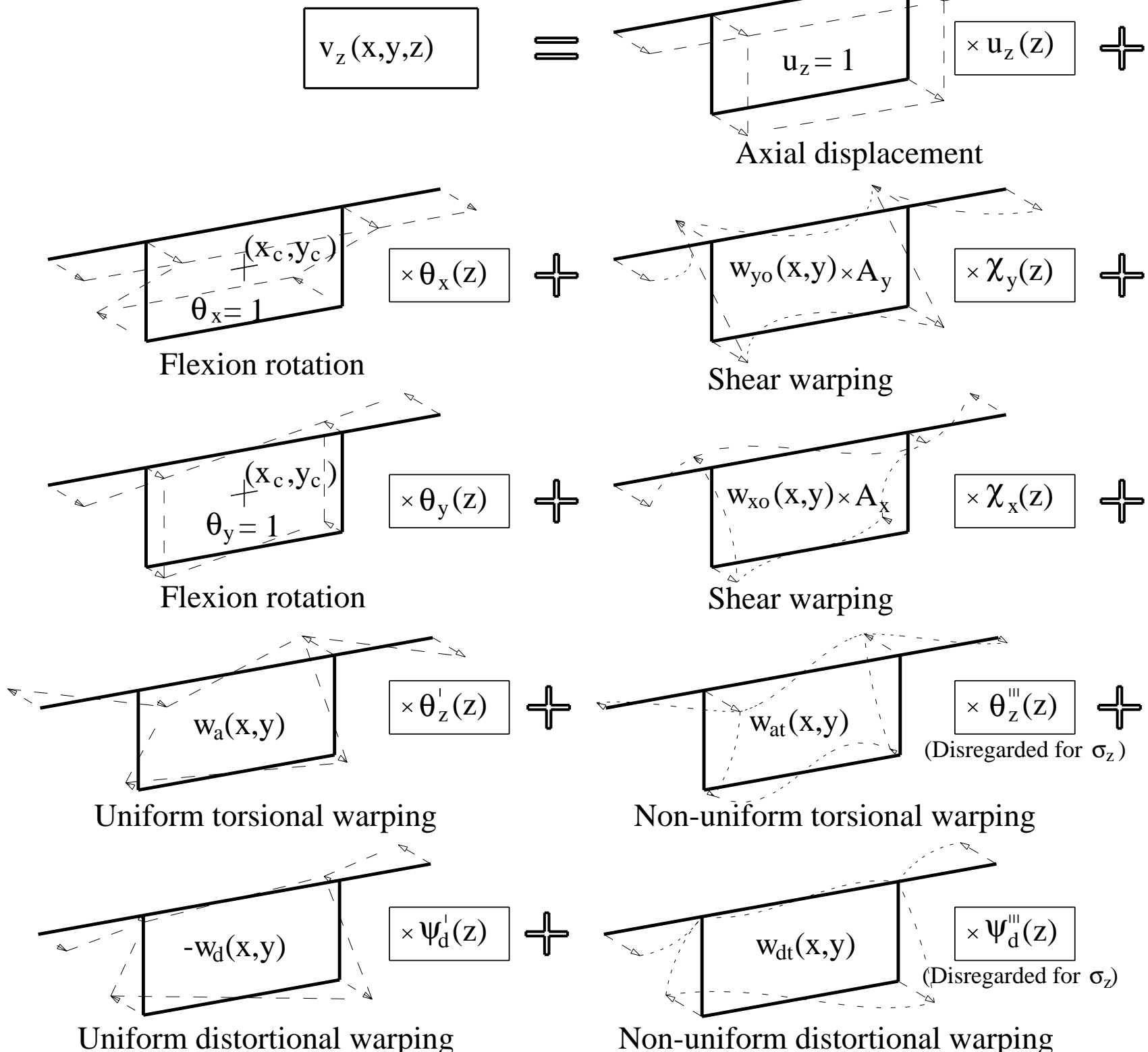








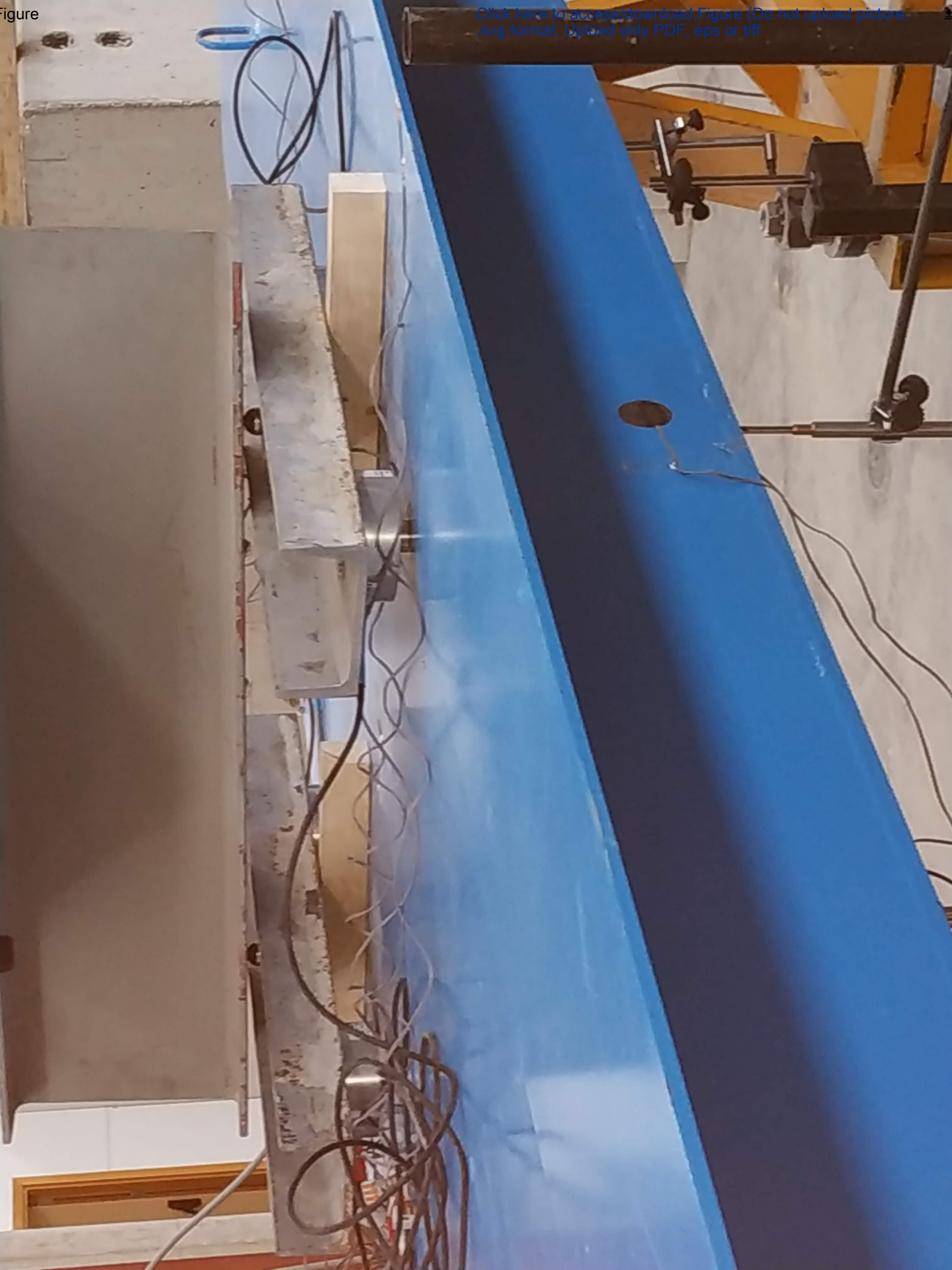


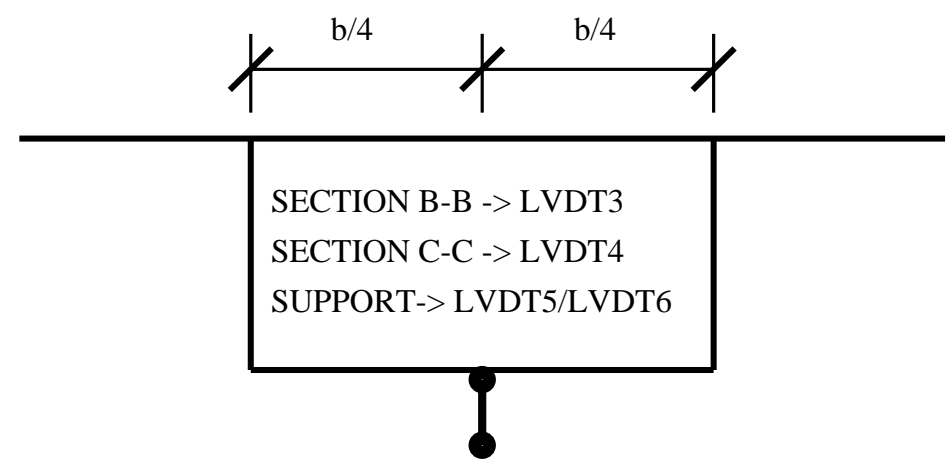
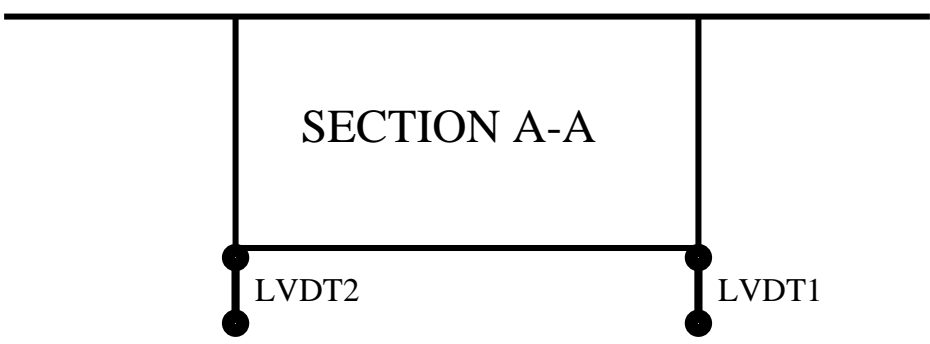
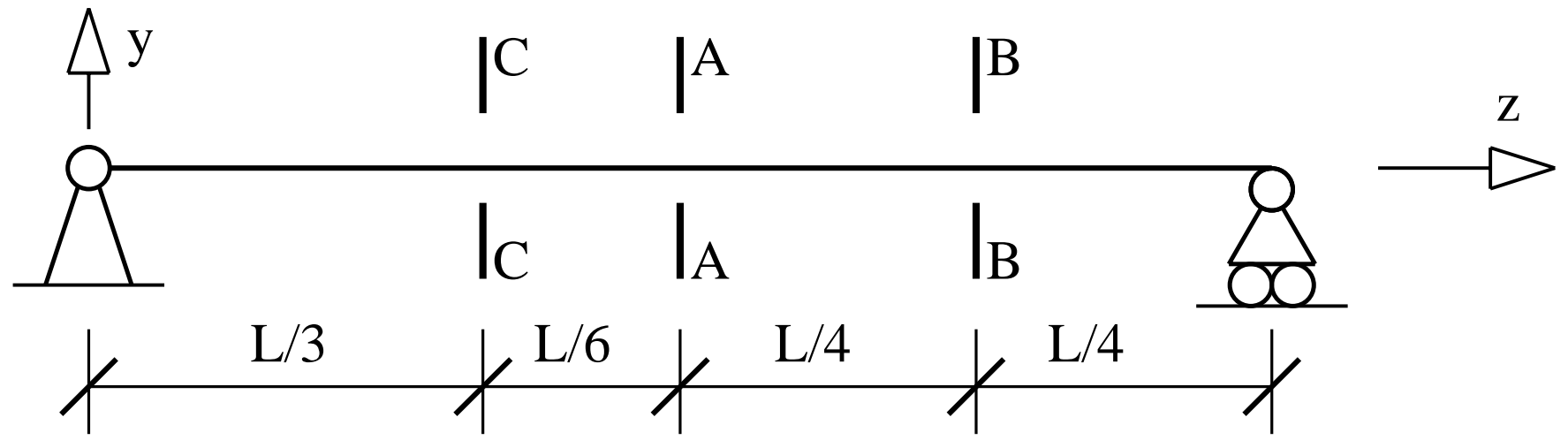


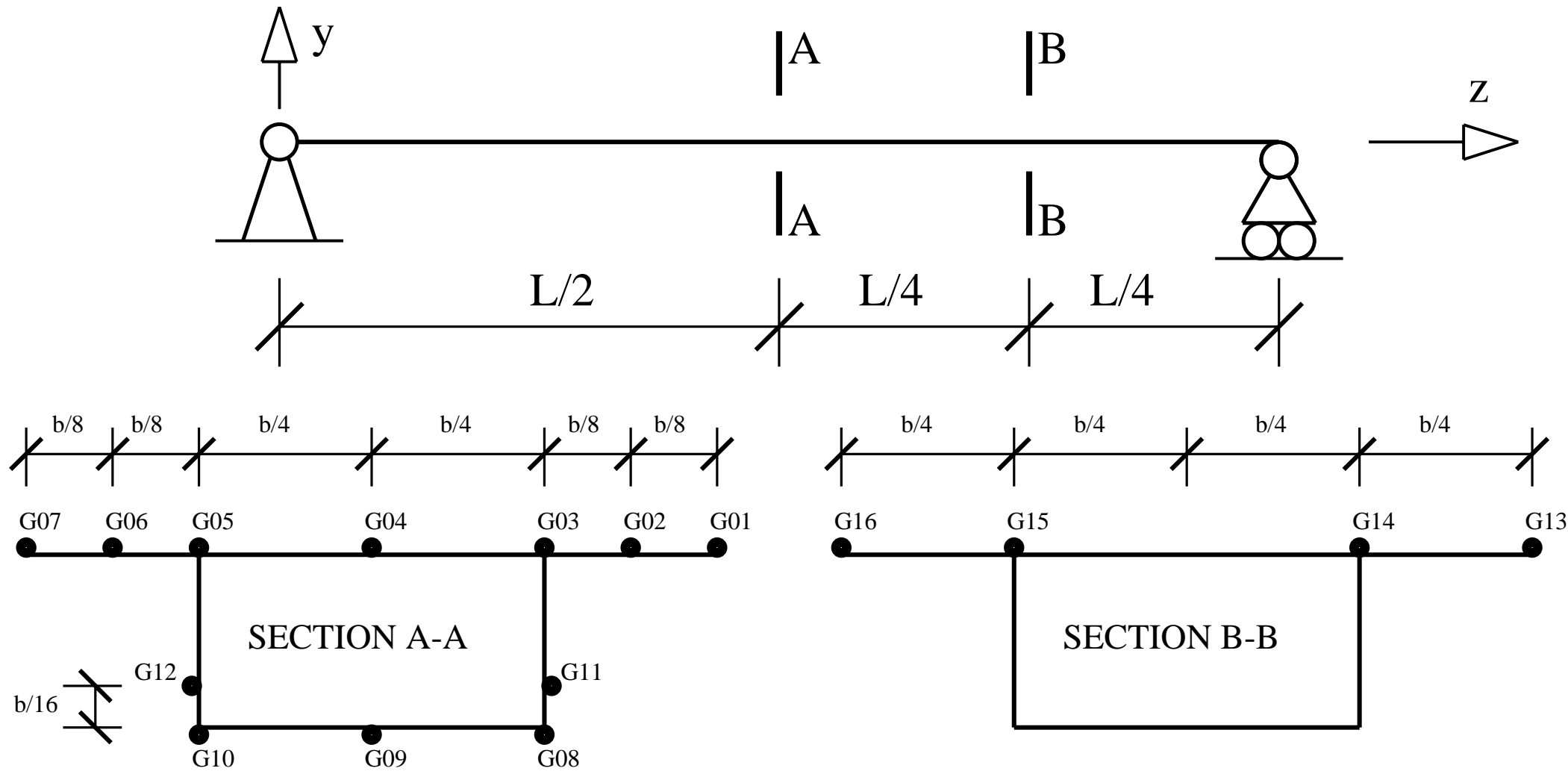
Figure

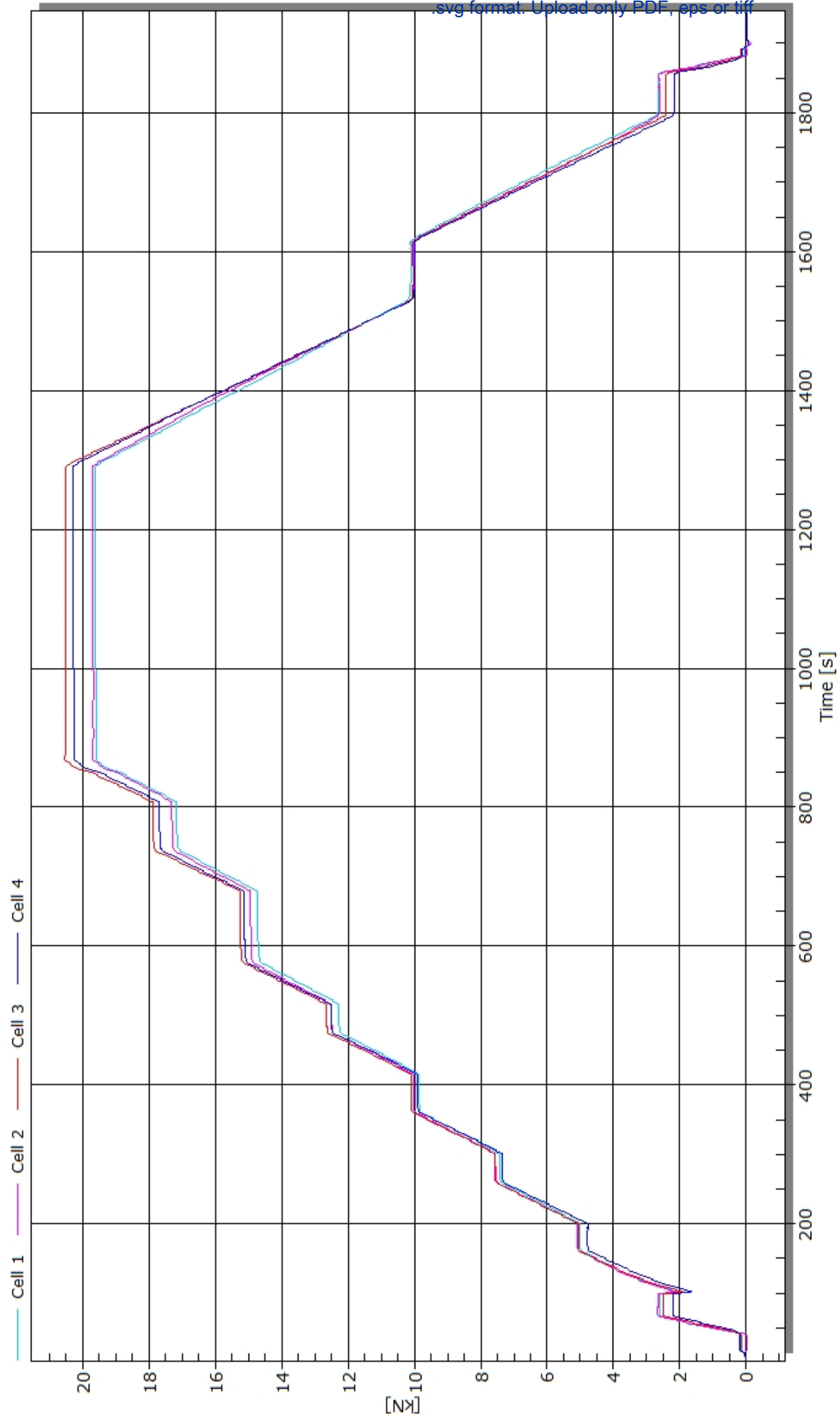
[Click here to access/download/figure](#) (Do not upload picture, svg format. Upload only PDF, eps or tiff)

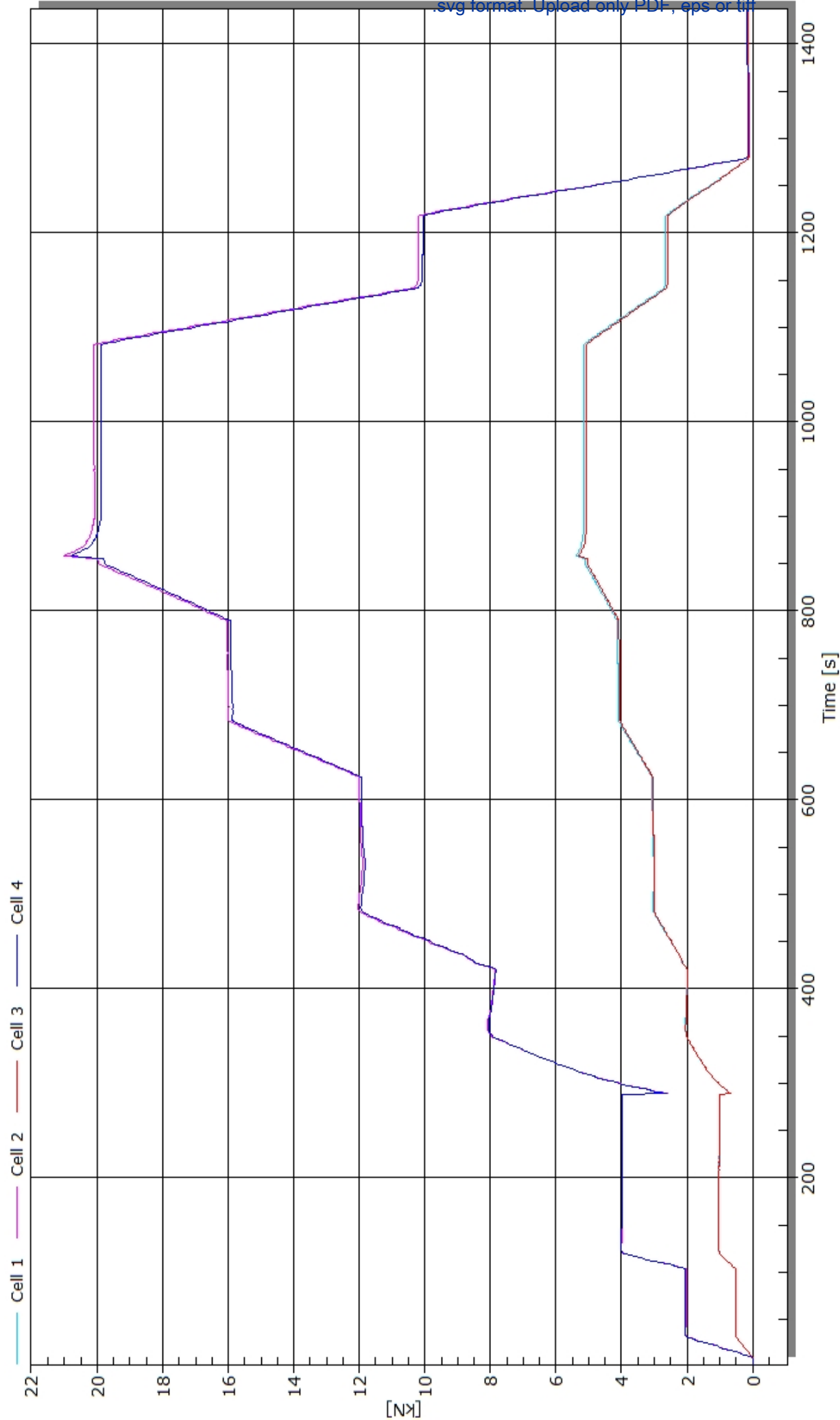


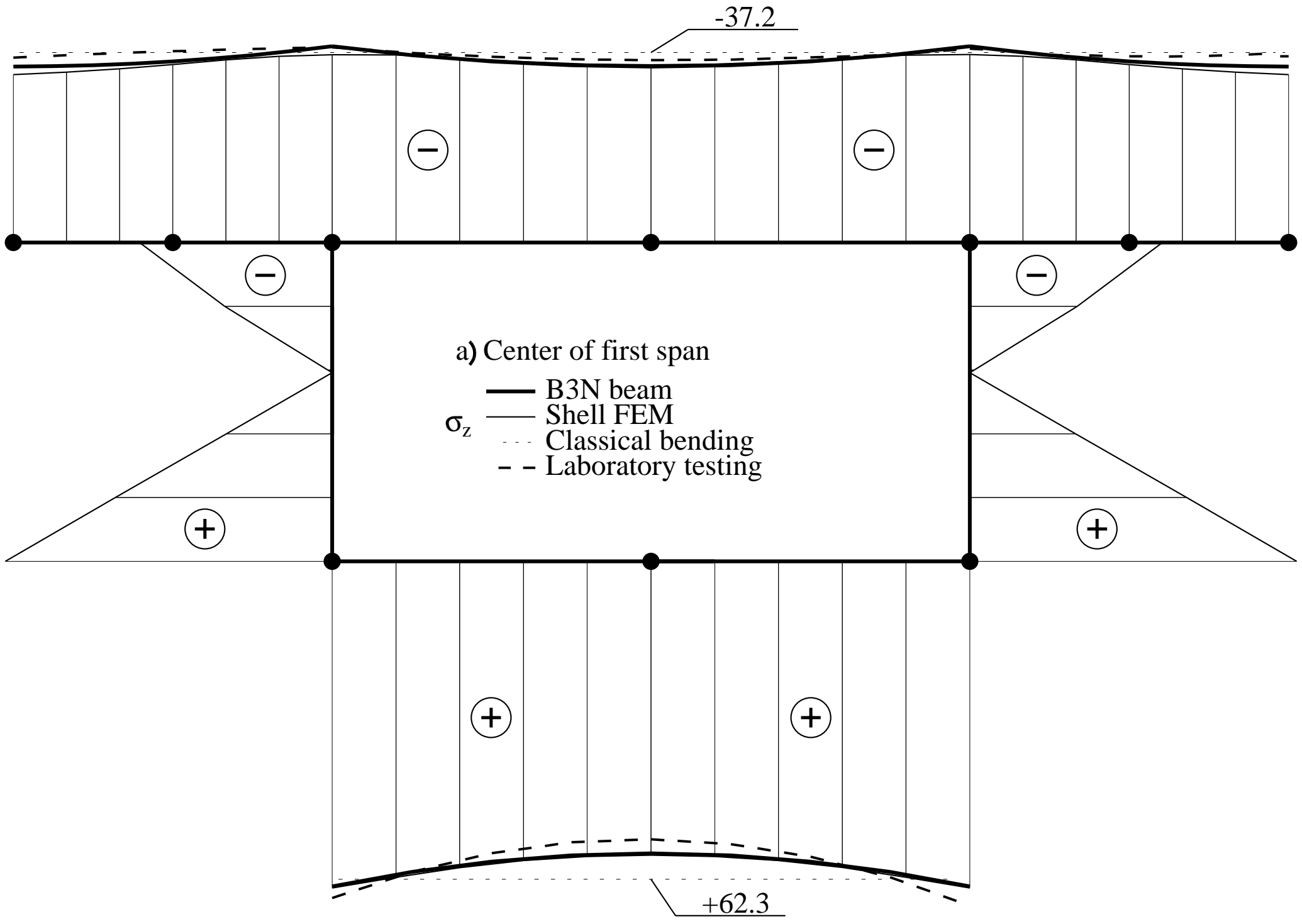


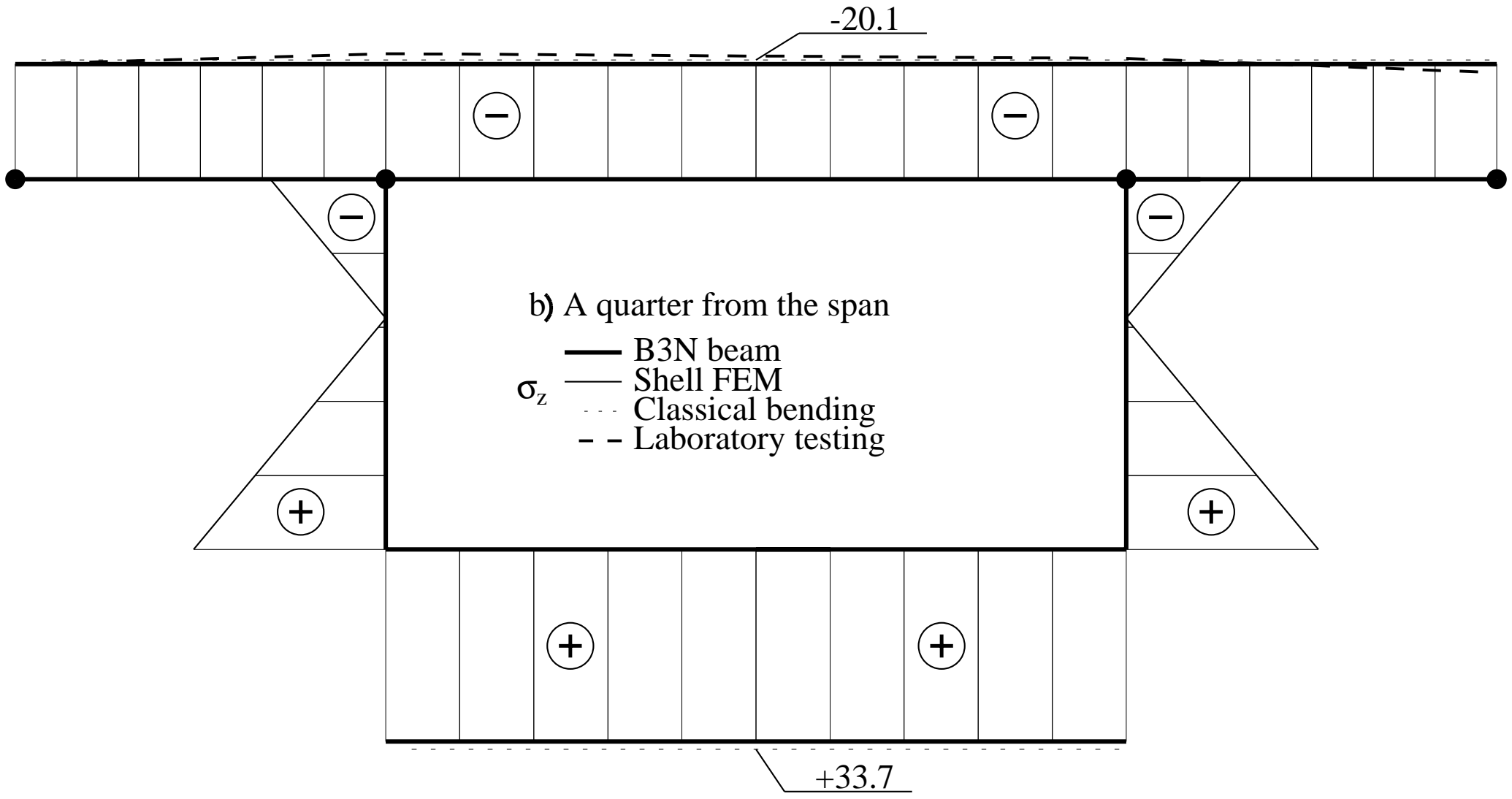


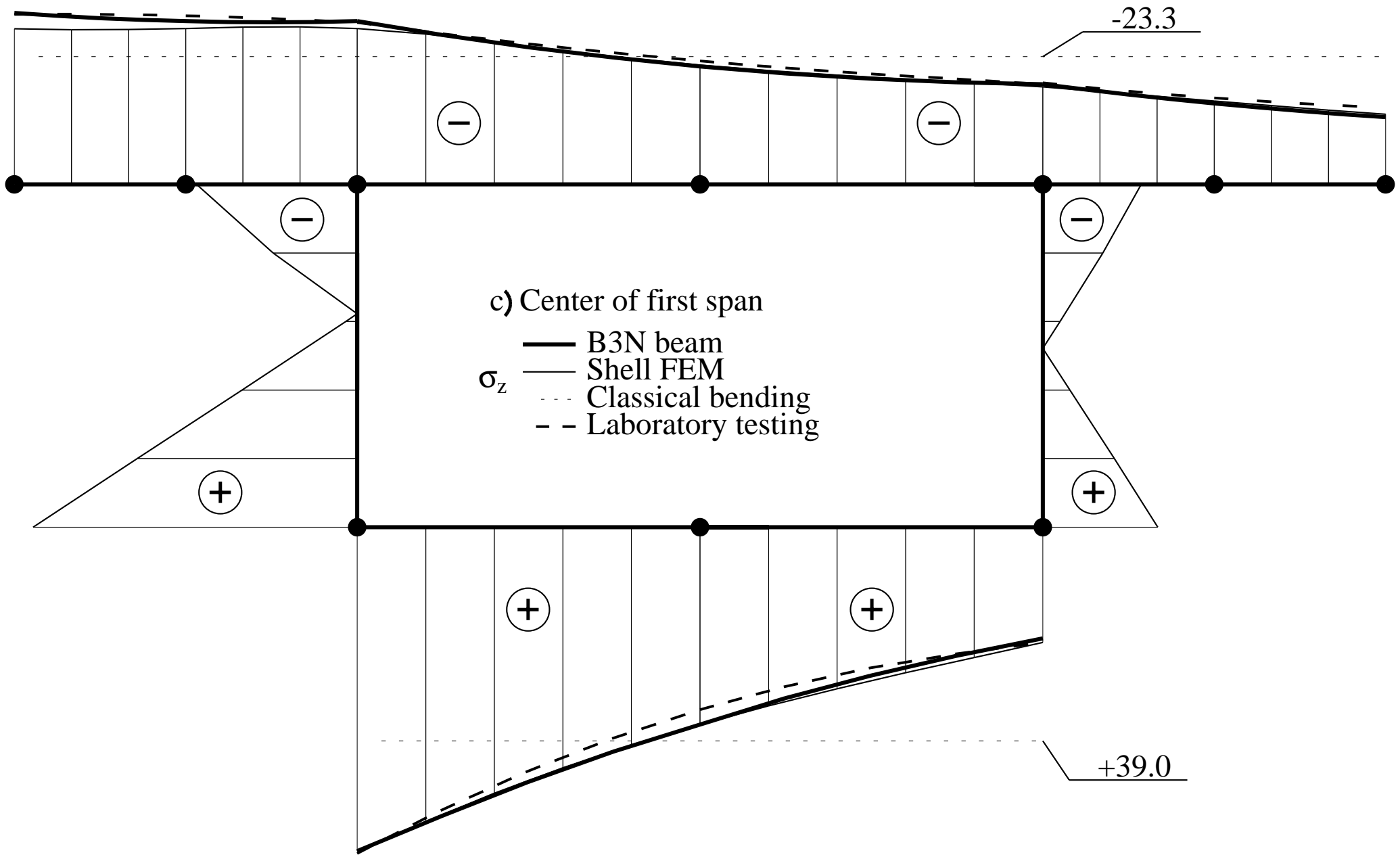


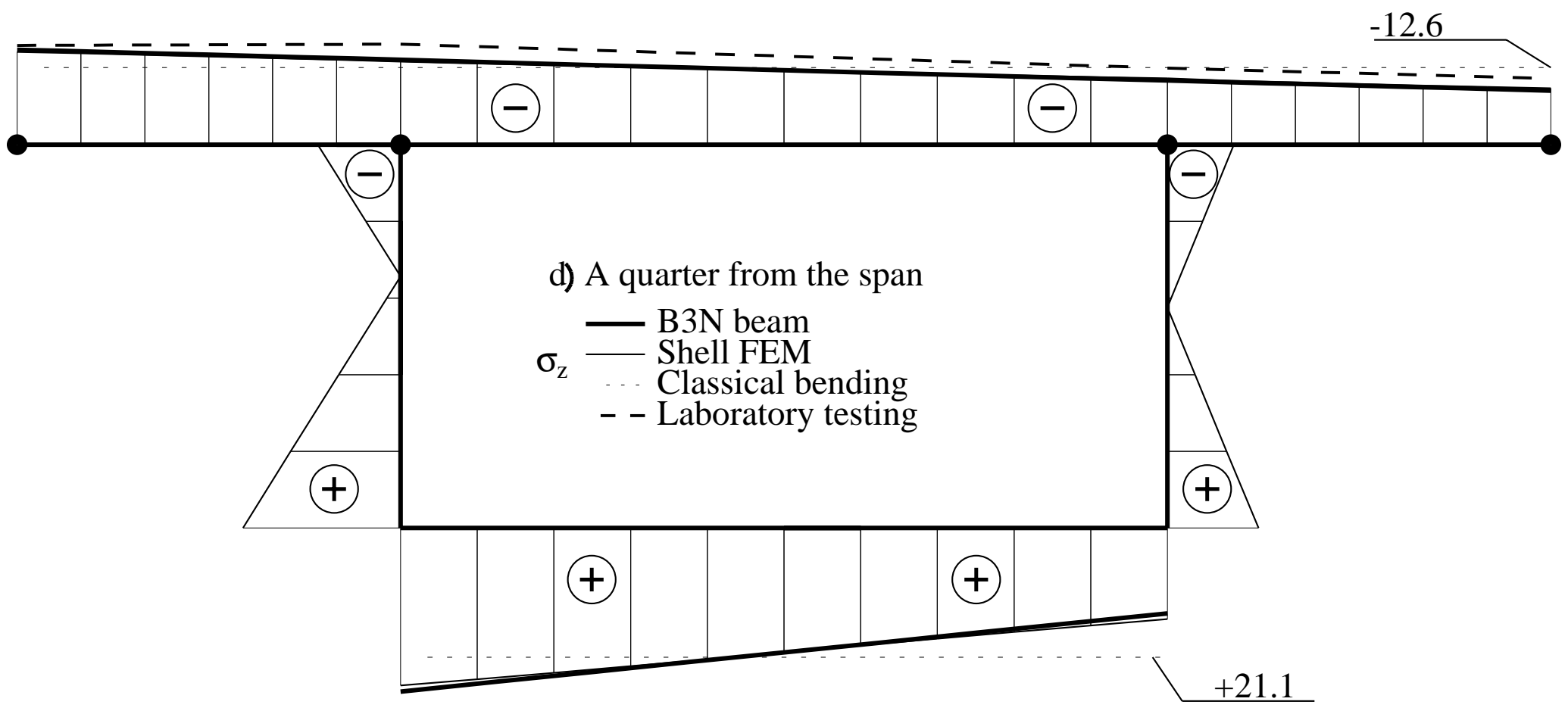


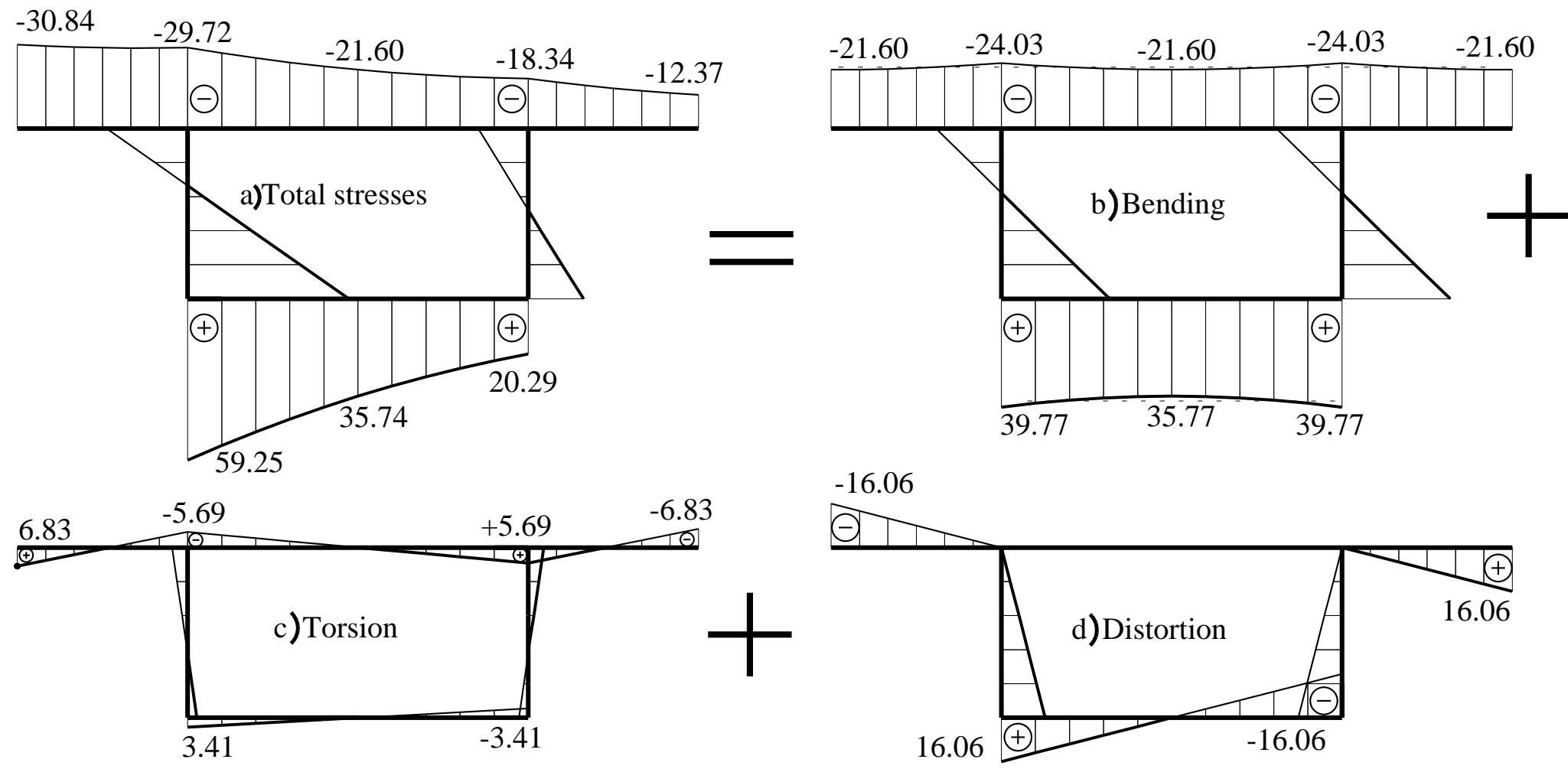


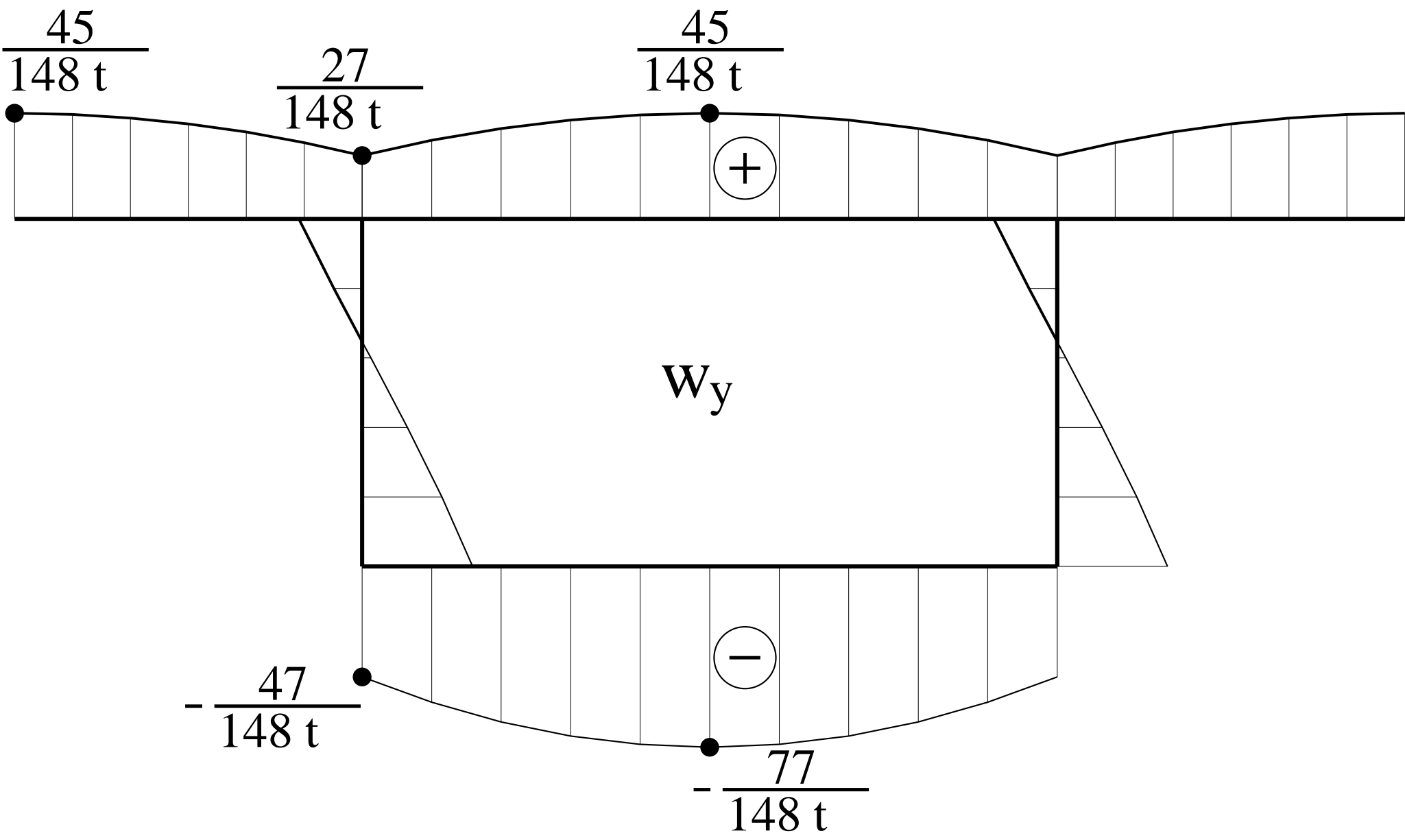


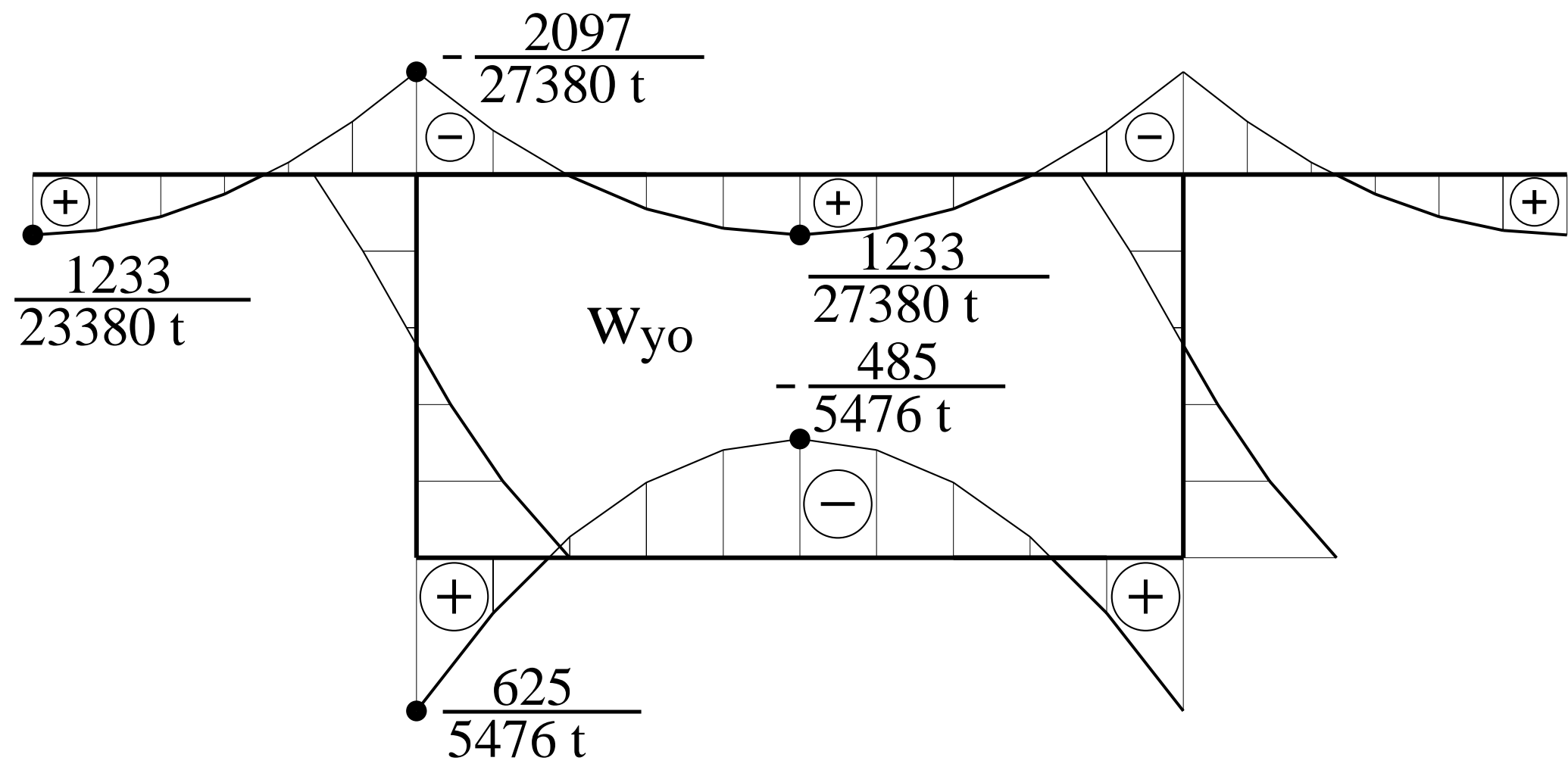


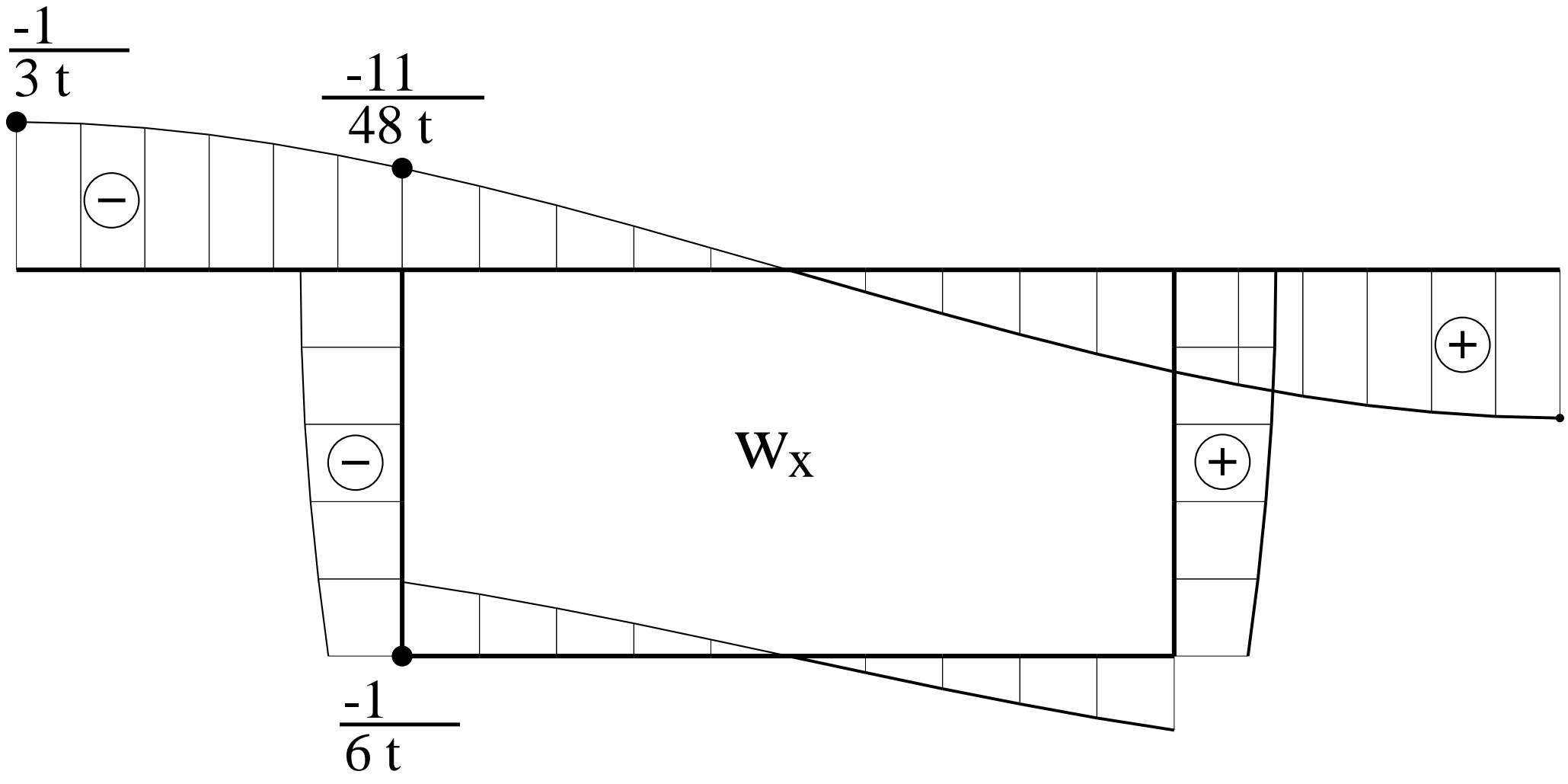


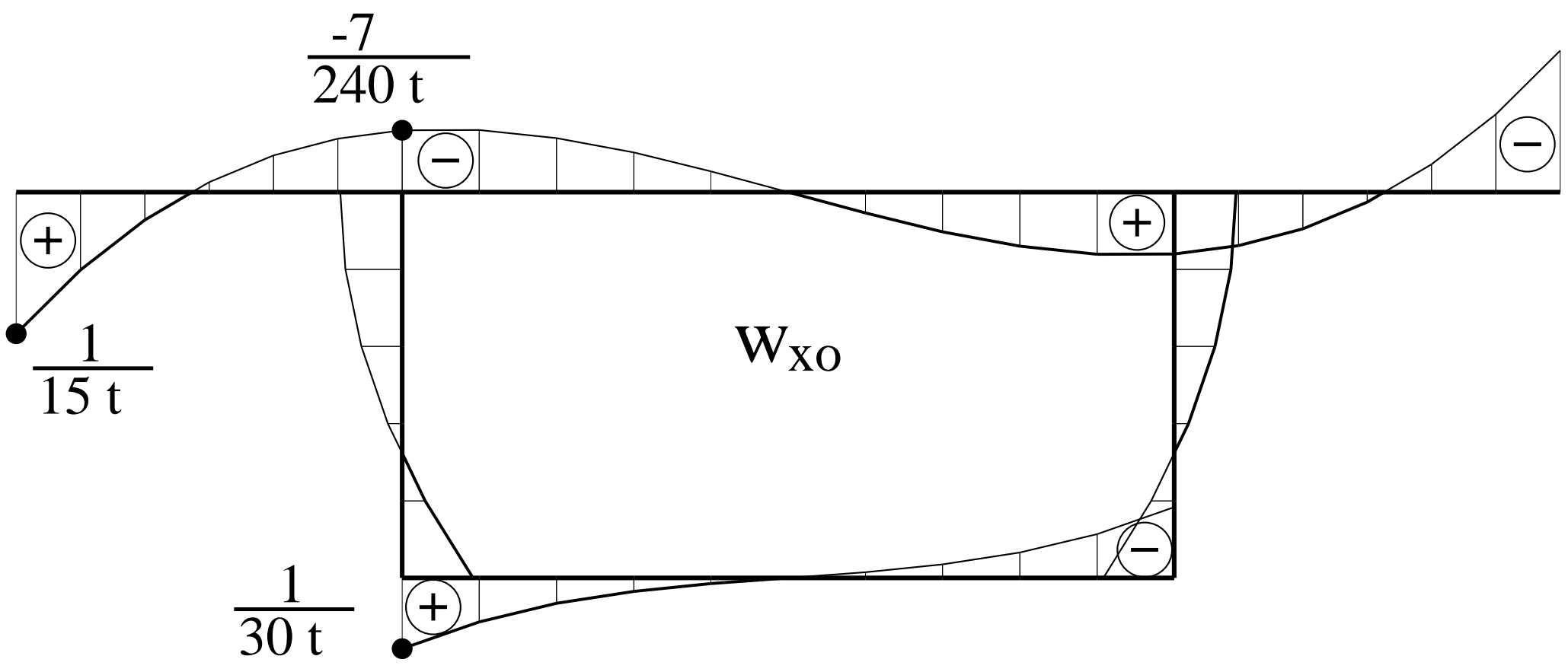


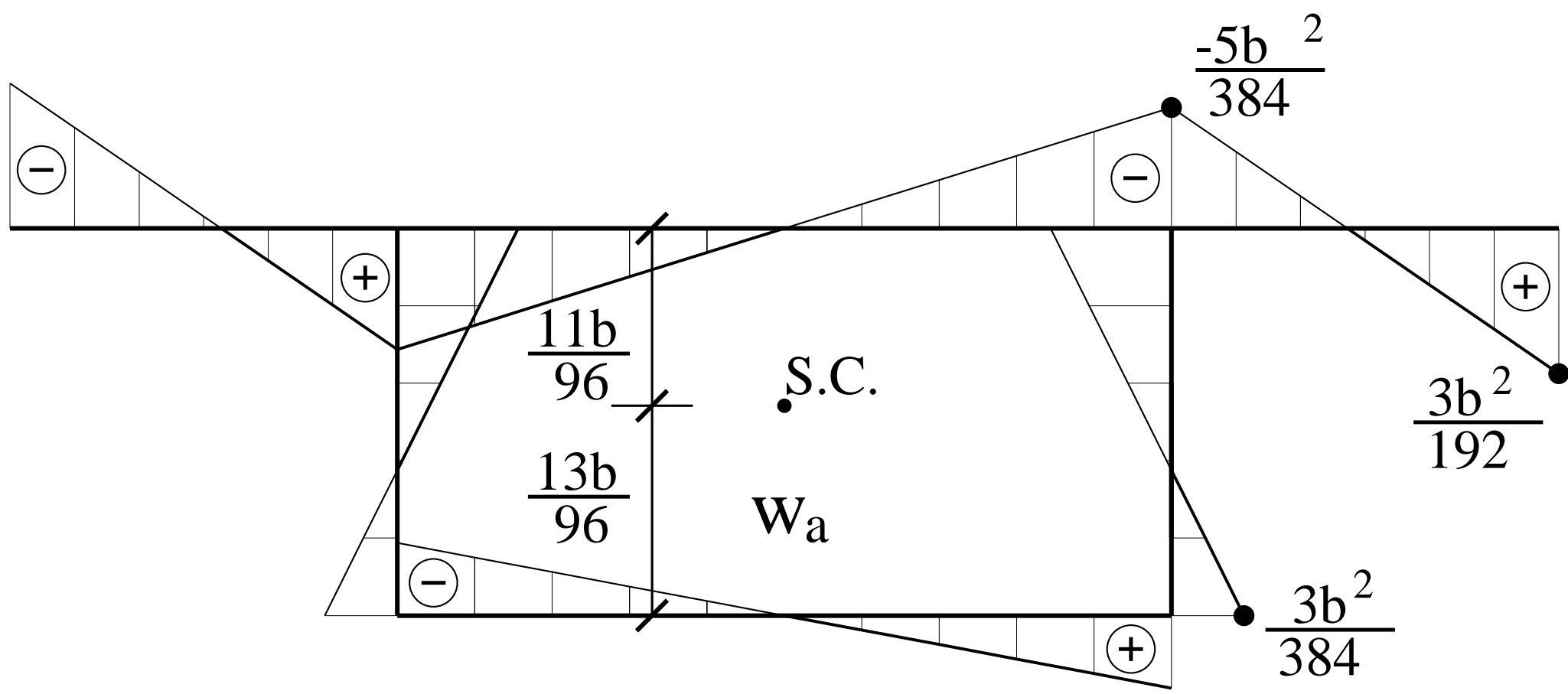


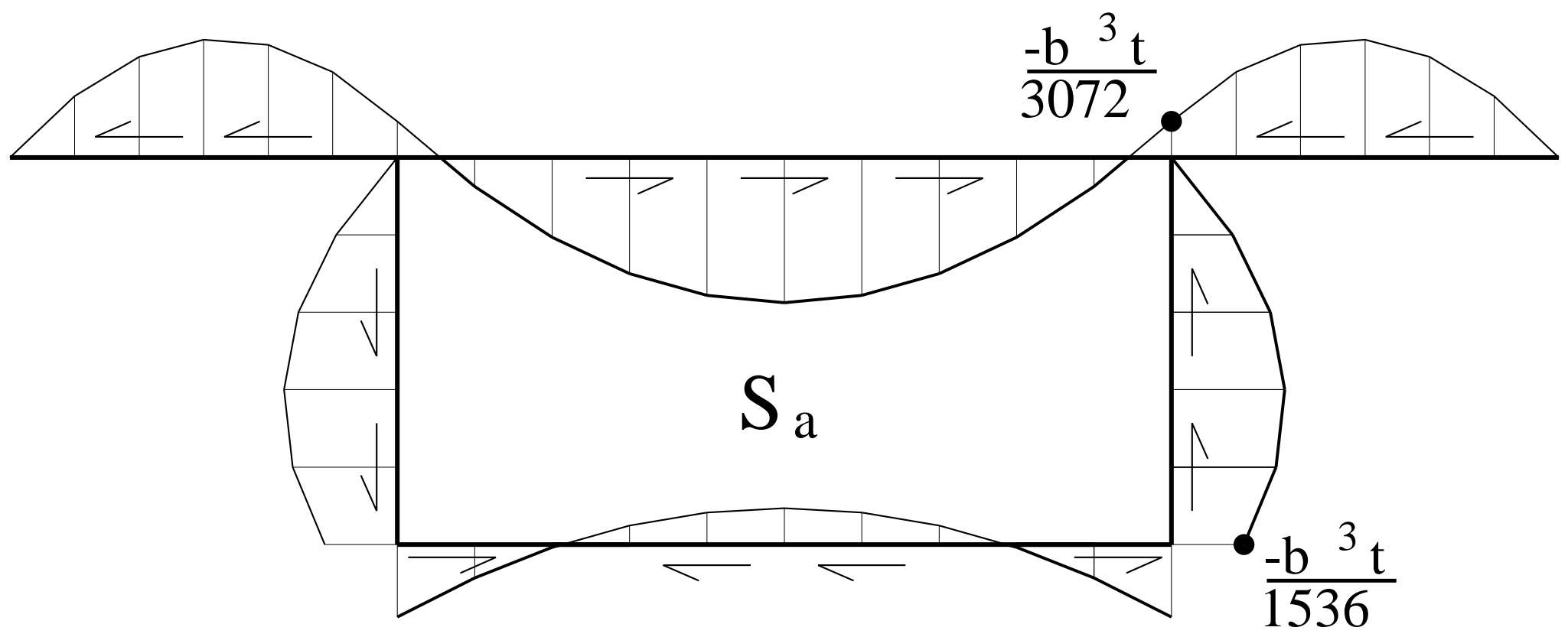


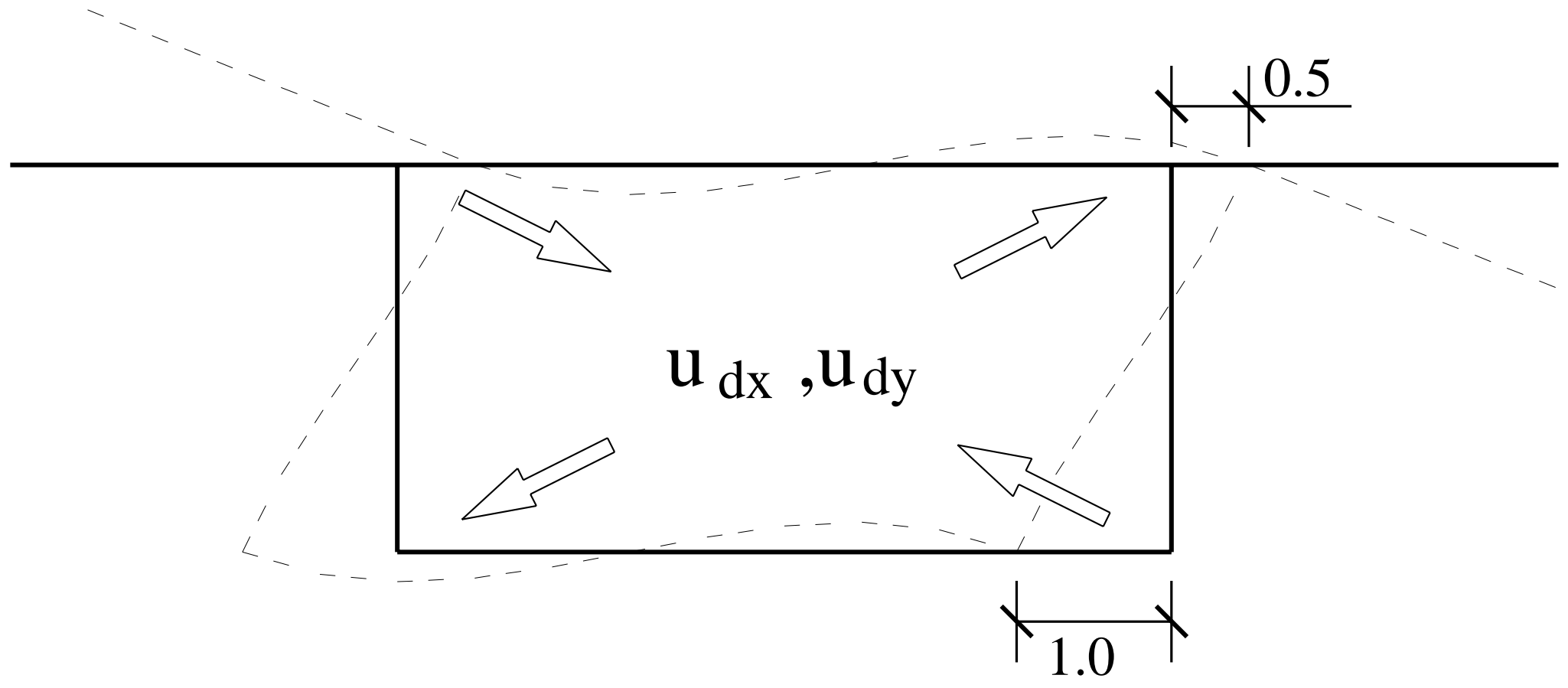


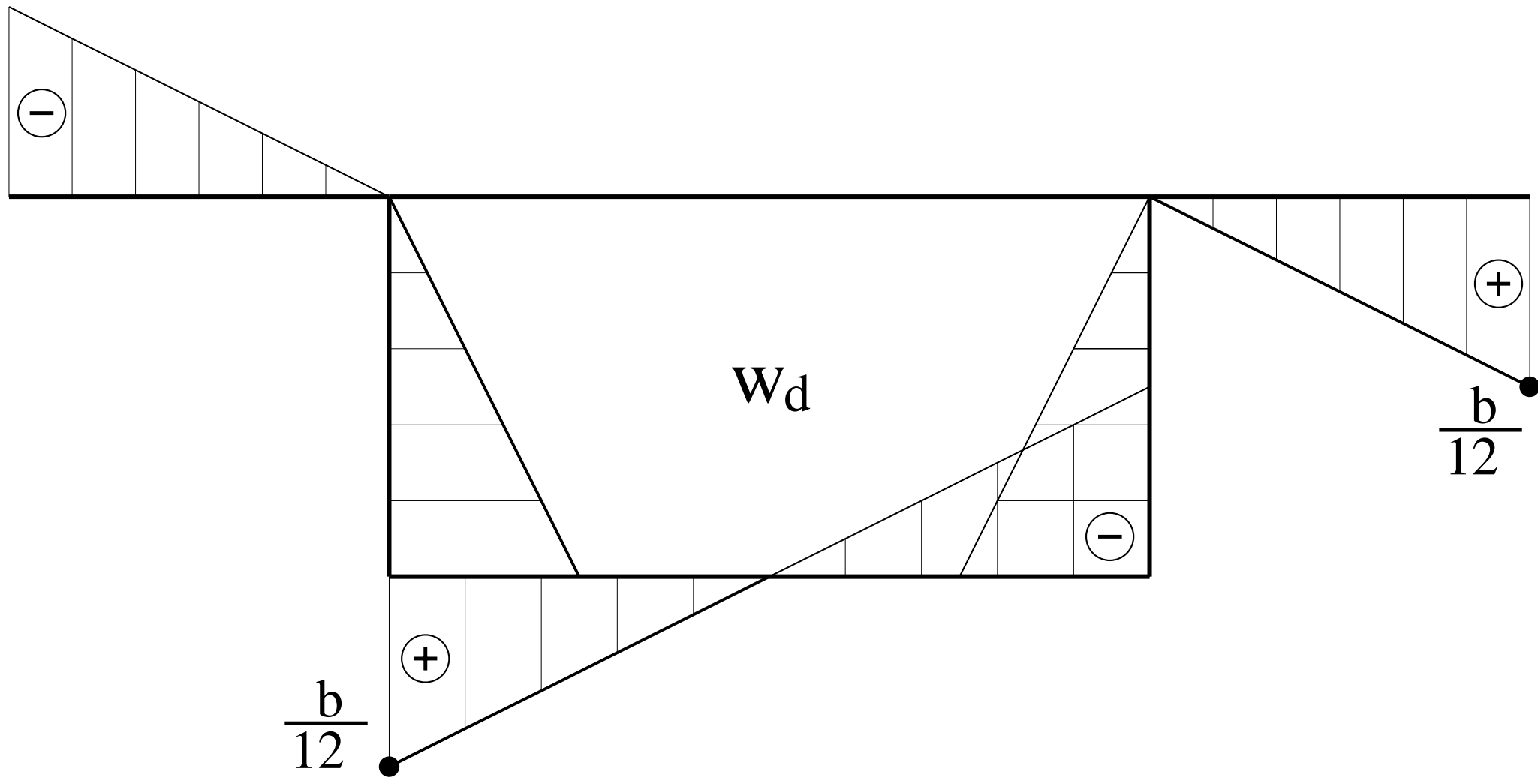


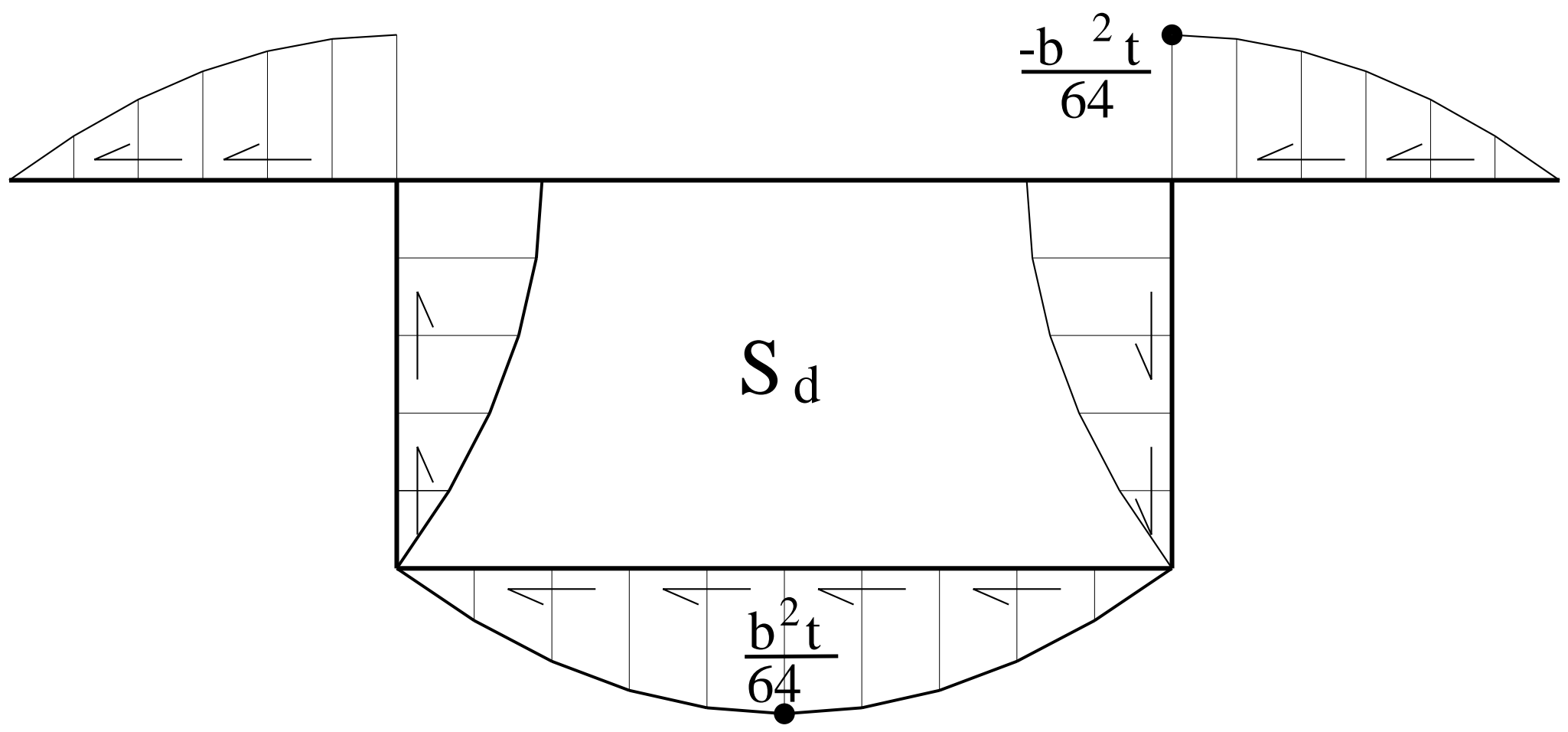


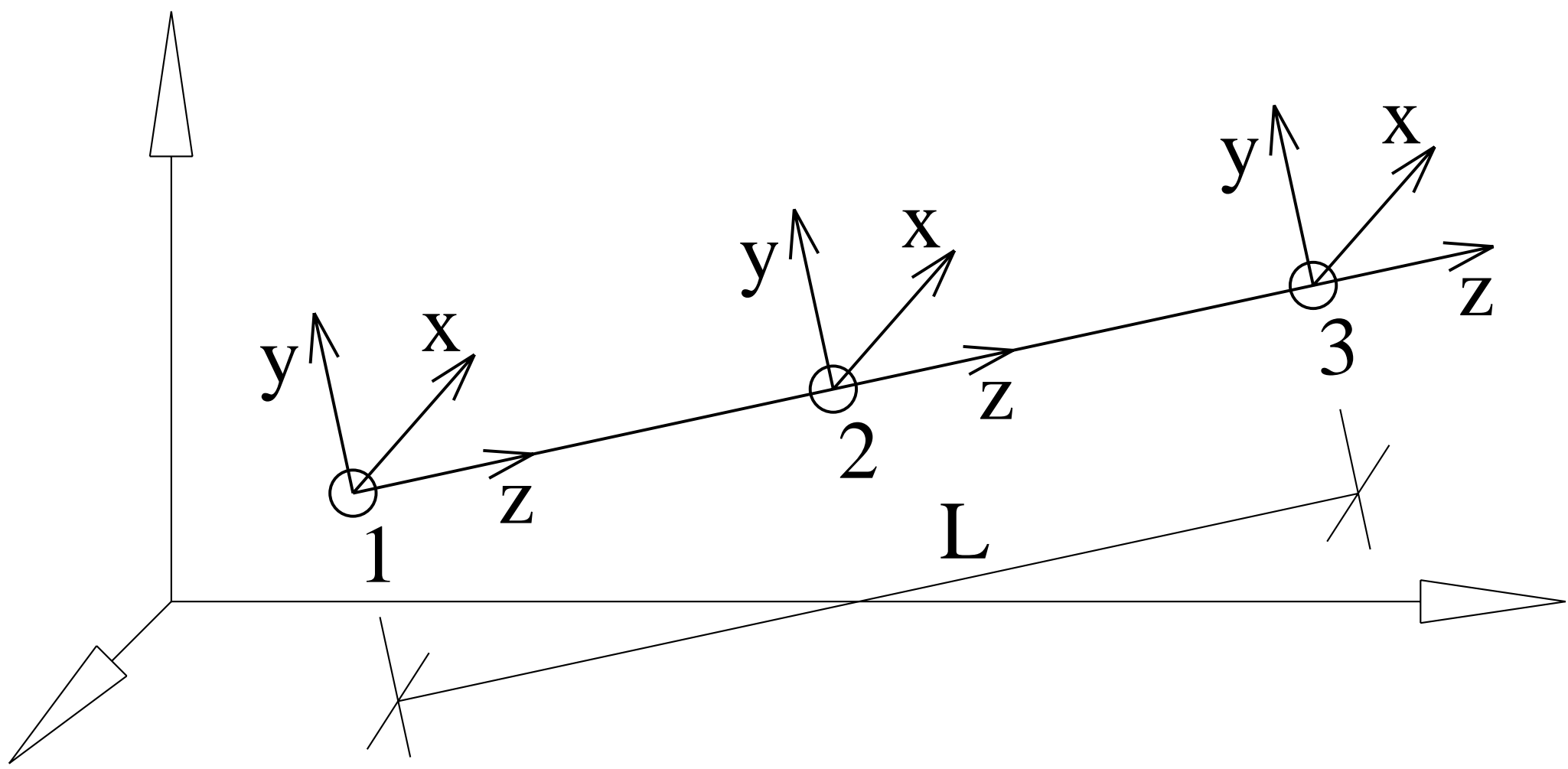




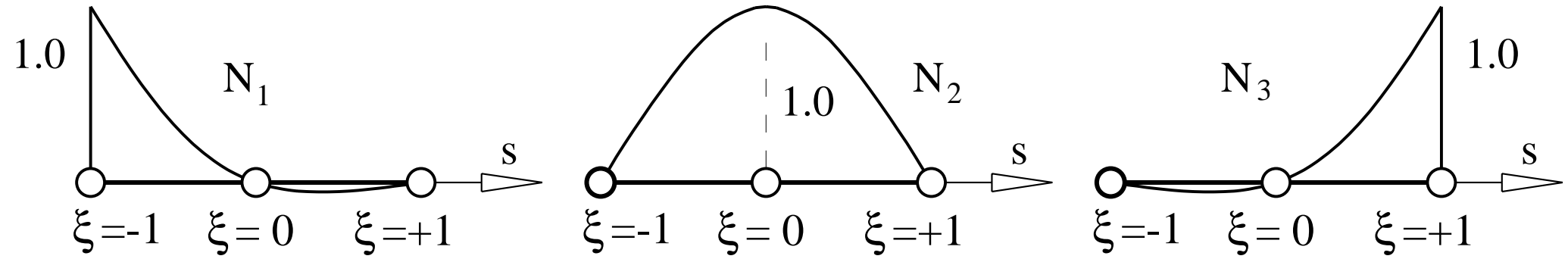




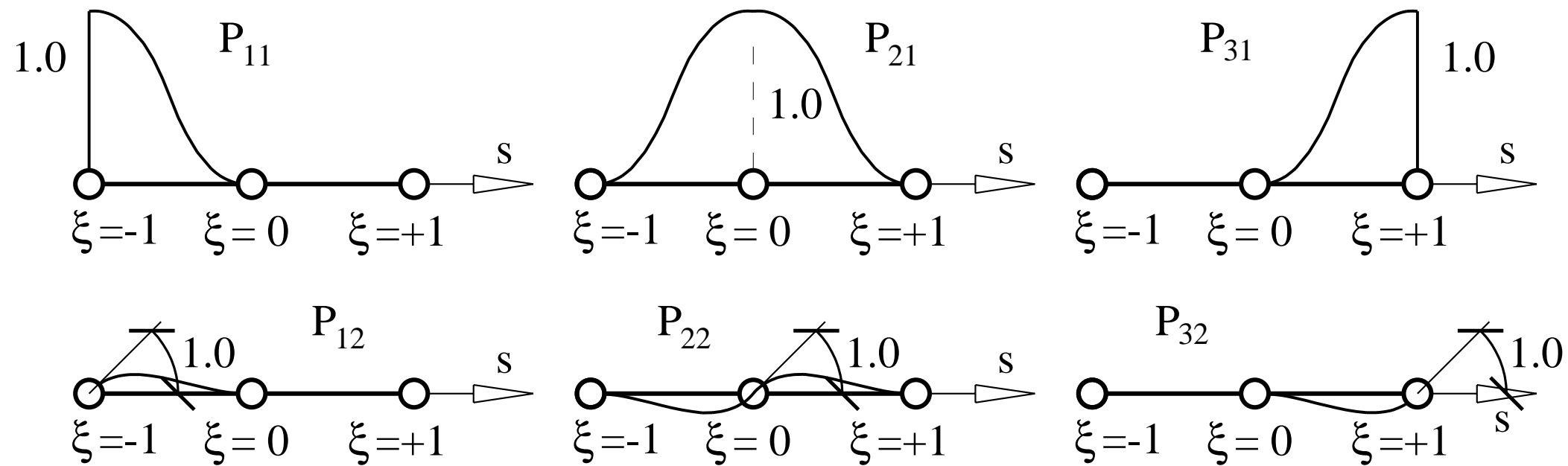




CONTINUITY C0

DOF: $u_x, u_y, u_z, \theta_x, \theta_y, \chi_x, \chi_y$ 

CONTINUITY C1

DOF: $\theta_z, \theta'_z, \Psi_d, \Psi'_d$ 

Declaration of interests

The authors declare that they have no known competing financial interests or personal relationships that could have appeared to influence the work reported in this paper.

The authors declare the following financial interests/personal relationships which may be considered as potential competing interests: